



OPEN ACCESS

EDITED BY

Glen T. Snyder,
The University of Tokyo, Japan

REVIEWED BY

Dong Feng,
Shanghai Ocean University, China
Firoz Badesab,
Council of Scientific and Industrial Research
(CSIR), India

*CORRESPONDENCE

Huiqiang Yao
✉ hqyao@163.com
Zijun Wu
✉ wuzj@tongji.edu.cn

RECEIVED 08 March 2023

ACCEPTED 13 December 2023

PUBLISHED 08 January 2024

CITATION

Chen Y, Xu S, Liu W, Zhang Z, Yang T, Xiao X,
Deng X, Li J, Yao H and Wu Z (2024)
Assessing biogeochemical controls on
porewater dissolved inorganic carbon cycling
in the gas hydrate-bearing sediments of the
Makran accretionary wedge, Northeastern
Arabian Sea off Pakistan.
Front. Mar. Sci. 10:1181921.
doi: 10.3389/fmars.2023.1181921

COPYRIGHT

© 2024 Chen, Xu, Liu, Zhang, Yang, Xiao,
Deng, Li, Yao and Wu. This is an open-access
article distributed under the terms of the
[Creative Commons Attribution License \(CC BY\)](https://creativecommons.org/licenses/by/4.0/).
The use, distribution or reproduction in other
forums is permitted, provided the original
author(s) and the copyright owner(s) are
credited and that the original publication in
this journal is cited, in accordance with
accepted academic practice. No use,
distribution or reproduction is permitted
which does not comply with these terms.

Assessing biogeochemical controls on porewater dissolved inorganic carbon cycling in the gas hydrate-bearing sediments of the Makran accretionary wedge, Northeastern Arabian Sea off Pakistan

Yuanqing Chen¹, Sinan Xu¹, Weining Liu¹, Zhen Zhang²,
Tianbang Yang², Xiao Xiao², Xiguang Deng², Jiangtao Li¹,
Huiqiang Yao^{2*} and Zijun Wu^{1*}

¹State Key Laboratory of Marine Geology, Tongji University, Shanghai, China, ²Key Laboratory of Marine Mineral Resources, Ministry of Natural Resources, Guangzhou Marine Geological Survey, China Geological Survey, Guangzhou, China

Quantitatively assessing the porewater dissolved inorganic carbon (DIC) cycling in methane-enriched marine sediments is crucial to understanding the contributions of different carbon sources to the global marine carbon pool. In this study, Makran accretionary wedge was divided into Zone 1 (high methane flux area) and Zone 2 (background area). Porewater geochemical compositions (Cl^- , SO_4^{2-} , NH_4^+ , Mg^{2+} , Ca^{2+} , Ba^{2+} , DIC and $\delta^{13}\text{C}$ -DIC) and a reaction-transport model were used to determine the DIC source and calculate the DIC flux through carbonate precipitation and releasing into overlying seawater in sediments. Zone 1 is characterized by the shallower depth of sulfate-methane transition (SMT), where most of porewater sulfate was consumed by anaerobic oxidation of methane (AOM). In contrast, a relatively low flux of methane diffusion in Zone 2 results in a deeper SMT depth and shallow sulfate is predominantly consumed by organoclastic sulfate reduction (OSR). Based on the porewater geochemical profiles and $\delta^{13}\text{C}$ mass balance, the proportions of porewater DIC originating from methane were calculated as 51% in Zone 1 and nearly 0% in Zone 2. An increase of porewater DIC concentration leads to authigenic carbonate precipitation. Solid total inorganic carbon (TIC), X-ray diffractometry (XRD) and scanning electron microscopy (SEM) analysis display that carbonate content increases with depth and aragonite appears at or below the depths of SMT. Meanwhile, the flux of DIC released from sediments calculated by the reaction-transport model is 51.3 ~ 90.4 mmol/m²-yr in Zone 1, which is

significantly higher than that in Zone 2 (22.4 mmol/m²·yr). This study demonstrates that AOM serves as the dominant biogeochemical process regulating the porewater DIC cycle, which has an important impact on the authigenic carbonate burial and the seawater carbonate chemistry.

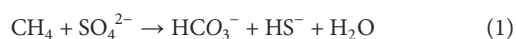
KEYWORDS

Makran accretionary wedge, anaerobic oxidation of methane (AOM), sulfate reduction, dissolved inorganic carbon (DIC), authigenic carbonate precipitation

1 Introduction

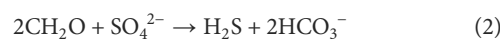
Methane (CH₄) seepage refers to methane-rich fluid leakage from the seabed, which is widely observed in active and passive continental margin slopes. The fluids show apparent spatial-temporal variations (Haas et al., 2010; Feng et al., 2016; Feng et al., 2020; Liu et al., 2020b; Wei et al., 2021), and often be accompanied by gas hydrate accumulations in areas of gas hydrate stability and where methane concentrations reach saturation (Milkov, 2004; Coffin et al., 2014; Mau et al., 2017; Feng et al., 2018; Zhang et al., 2021a). Under the driving force of geological structure, pressure or temperature changes, the gas hydrate can dissociate and increase the intensity of gas seeps, thereby significantly affecting benthic biogeochemical processes that control the highly spatially heterogeneous seafloor ecosystems (Suess, 2014; Liu et al., 2020a; Liao et al., 2022).

Although the CH₄ carbon estimates of hydrate-bound gas in global marine sediments are thought to be highly uncertain, the current estimate is widely believed to range from 1000 to 2500 Gt (Kvenvolden, 1988; Lerche, 2000; Milkov, 2004; Kretschmer et al., 2015). This buried organic carbon reservoir greatly exceeds many other reservoirs such as marine dissolved materials (980 Gt), terrestrial biota (830 Gt), the atmosphere (3.6 Gt) and marine biota (3 Gt) in the global carbon cycle (Kvenvolden, 1988). The dissociation of gas hydrates will result in the consequent liberation of various carbonaceous compounds such as CH₄, CO₂, and HCO₃⁻ (Suess et al., 1999; Phrampus and Hornbach, 2012). Previous studies have shown that more than 90% of the CH₄ is consumed through anaerobic oxidation of methane (AOM) in marine sediments (e.g., Boetius et al., 2000; Haese et al., 2003; Chen et al., 2021; Wei et al., 2021; Li et al., 2023), which effectively prevents the diffusion of dissolved CH₄ into overlying seawater or even the atmosphere. The AOM is mainly coupled to the sulfate reduction and occurs at a distinct zone which is known as the sulfate-methane transition (SMT) in the sediments (Equation 1) (Reeburgh, 1976; Borowski et al., 1996; D'Hondt et al., 2002; Snyder et al., 2007).

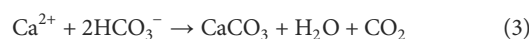


The upward flux of methane is theoretically nearly equal to the downward diffusive sulfate flux within the SMT due to the

stoichiometric ratio of 1:1 between SO₄²⁻ and CH₄ in the AOM (Niewöhner et al., 1998; Knittel and Boetius, 2009; Akam et al., 2020). However, the calculated downward diffusive sulfate flux often exceeds that of the upward flux of methane (e.g., Wu et al., 2016; Akam et al., 2020; Zha et al., 2022). A compilation by Egger et al. (2018) from 740 sites covering a wide range of oceanic conditions observed the global mean net flux ratio between SO₄²⁻ and CH₄ of 1.4:1. This observed flux imbalance can be attributed to the organoclastic sulfate reduction (OSR) through the oxidation of buried organic matter (Berner, 1980; Jørgensen et al., 2019; Chen et al., 2020; Zha et al., 2022), and the reaction is represented in very simple form as Equation 2:



Both the microbially-mediated AOM and OSR can generate dissolved inorganic carbon (DIC) and increase porewater alkalinity (Equations 1, 2), thus leading to the promotion of authigenic carbonate precipitation (Equation 3) (Chatterjee et al., 2011; Smith and Coffin, 2014; Chen et al., 2023).



It should be pointed out that other alkaline earth elements such as Mg, Sr, Ba, and Fe can substitute for Ca in varying amounts during the process of carbonate precipitation (Equation 3). In addition to being removed by carbonate precipitation, a portion of the porewater DIC will migrate toward the seafloor and finally enter the overlying seawater (e.g., Smith and Coffin, 2014; Graves et al., 2015; Feng et al., 2020). Therefore, quantitative assessment of the porewater DIC cycle in marine sediments is crucial for better understanding the global authigenic carbonate burial and seawater carbonate chemistry.

The DIC concentration and its isotopic composition (δ¹³C-DIC) in porewater serve as sensitive indicators of the alteration of carbon species in marine sediments (Chen et al., 2010; Feng et al., 2020; Zha et al., 2022). Previous studies of DIC concentration and its δ¹³C-DIC have quantitatively tracked various sources, sinks, and transformation terms using the end-member isotopic compositions of various carbon pools (e.g., Aller and Blair, 2004; Formolo et al., 2004; Winde et al., 2014; Wu et al., 2016). Due to the high spatial and temporal heterogeneity of methane turnover above the gas

hydrate stability zone (GHSZ), it is necessary to conduct geochemical investigations of the dissolved species found in the porewater of closely associated marine sediments. These resulting geochemical data will help constrain the cycling and fate of DIC related to diagenetic processes in marine sediments with similar continental margin environments, and thus contribute to ascertaining global carbon flux in these settings.

Methane seepage and obvious gas emissions widely occur on the continental slope of the Makran accretionary wedge off Pakistan (von Rad et al., 2000; Delisle and Berner, 2002; Fischer et al., 2012; Wei et al., 2021). Existing works have mainly focused on the use of geophysical methods to identify the distribution and reserves of methane hydrate in this area (von Rad et al., 2000; Römer et al.,

2012; Wei et al., 2021; Wu et al., 2021). The conversion of methane carbon to DIC by geochemical processes in the Makran accretionary wedge was rarely reported and in particular, the quantitative assessment of the DIC cycle was not involved. In 2018, China Geological Survey carried out a China - Pakistan joint marine scientific cruise on the Makran continental margin offshore Pakistan (Figure 1A). The hydroacoustic evidence for Bottom Simulating Reflections (BSRs) indicates significant methane-hydrate burial in the study area (e.g., Wei et al., 2021; Wu et al., 2021; Zhang et al., 2021b). In this study, we collected six sediment gravity cores and analyzed the porewater geochemical composition (e.g., Cl^- , SO_4^{2-} , NH_4^+ , Ca^{2+} , Mg^{2+} , Ba^{2+} , DIC and $\delta^{13}C-DIC$), total organic carbon (TOC) and carbonate phase

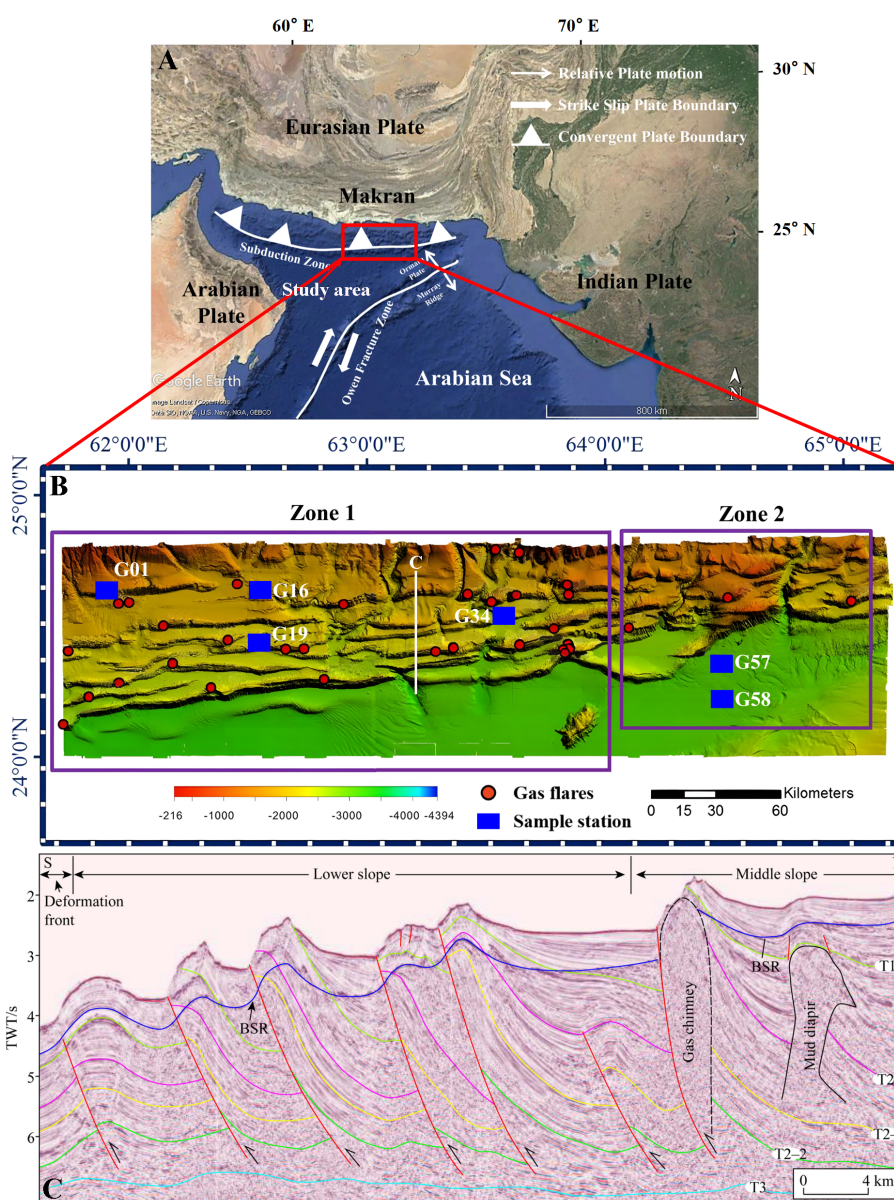


FIGURE 1 The maps of the study area and sampling sites. (A) Study area and its related tectonic setting; (B) Sampling sites and bottom topography of the investigated area. The stations with gas flares are referred to Wei et al. (2021). White line is the track line of the seismic profiles panel (C); (C) Multi-channel seismic data shows the occurring of bottom simulating with reversed polarity (BSR) in the study area (Zhang et al., 2020).

compositions. Our aims are to determine the source of DIC, the relative contributions of different geochemical processes (AOM vs. OSR) to the porewater DIC pool, and quantitatively assess the fate of DIC in the study area using the reaction-transport model.

2 Study location and methodology

2.1 Study area

The study area is located in the Makran accretionary wedge of the northern Indian Ocean, which has a complex thrust structure and the lowest subduction angle worldwide (about 3°) (Kopp et al., 2000; Wu et al., 2021) (Figure 1A). Shallow gas accumulates and moves along normal faults in abundant anticlinal hinges created by the highest subducted sediments, resulting in seepage to the seafloor (Römer et al., 2012; Himmler et al., 2015; Liao et al., 2022). Seismic data revealed widespread distributions of BSRs in the slope area across the Makran continental margin (Figure 1C), indicating the widespread occurrence of gas hydrates in this area (e.g., Grando and McClay, 2007; Zhang et al., 2020; Liao et al., 2022). Various types of faults, mud diapirs, gas chimneys, and associated diapiric structures provide conduits for methane seepage in the Makran (von Rad et al., 2000; Schlüter et al., 2002; Khan et al., 2020; Wei et al., 2021; Wu et al., 2021; Liao et al., 2022). Methane seepage has been discovered ubiquitously (Römer et al., 2012), accompanied by cold seep ecosystems (Fischer et al., 2012) and authigenic carbonates (Himmler et al., 2015).

2.2 Sample collection

From December 2018 to February 2019, a systematic multi-beam sonar survey for gas emissions was conducted with the R/V “Haiyangdizhi 10” during a scientific diving expedition of the Makran accretionary wedge off Pakistan (Wu et al., 2021). Based on active flare density and methane seepage intensity, six sediment gravity cores with lengths ranging from 355 to 835 cm were recovered in two zones: Zone 1 (sites G01, G16, G19, and G34) has a high methane flux and a water depth of 500–2500 m; Zone 2 is the background area near Zone 1, with a water depth greater than 3000 m. In terms of geological structure, Zone 1 is heavily transected by imbricate faults and accretionary structures, while the forearc area is largely intact in deeper Zone 2 (Figure 1B).

After being retrieved, the core was promptly transported to the onboard laboratory for the purpose of collecting methane and extracting porewater. Sediment samples for methane analysis (3 ml) were taken using a 10 ml cut syringe and immediately transferred into 10 ml headspace vials, which contained 3 ml of 1 mol/l NaOH solution. The vials were subsequently capped with a rubber septum and sealed with a crimper, stored at low temperatures for the determination of sediment CH₄ concentration. Porewater samples were collected at 60 cm intervals using Rhizon samplers according to the procedure presented by Liu et al. (2020a). The porewater samples were then immediately chemically treated and preserved for a variety of

analysis purposes. The solid phase was divided into sub-samples at 10 cm intervals and stored at –20 °C for further analysis.

About 2 ml of porewater subsamples for cations (Ca²⁺ and Mg²⁺) and anions (SO₄²⁻ and Cl⁻) analysis was acidified with 20 µl 65% HNO₃ (suprapure, Merck) to prevent precipitation and sulfur oxidation. Samples for porewater NH₄⁺ analysis were preserved in a 2 ml PE tube and frozen. Subsamples for measurements of DIC concentration and its isotopic composition were stored in 3 ml Labco anaerobic flasks without a headspace and kept at 4 °C in the research vessel's cold room. Once on land, these samples were immediately placed in a refrigerated case and shipped to the onshore laboratories for further analysis within 4 weeks.

2.3 Analytical methods

2.3.1 Chemical and isotopic analysis of porewater

Dissolved Ca²⁺, Mg²⁺ and Ba²⁺ concentrations were diluted at 1:30 with 18-MΩ water and measured with inductively coupled plasma atomic emission spectroscopy (ICP-AES; IRIS Advantage, Thermo Jarrell Ash). Scandium (0.5 mg/L) was added to both standards and samples for correcting signal drift during instrument operation. Porewater samples were diluted with 2% subboiled HNO₃ along with reference materials (CASS-4) from the National Research Council of Canada (NRCC). The accuracy and precision were better than ± 5%.

Porewater samples for SO₄²⁻ and Cl⁻ concentrations were diluted at 1:250 using 18-MΩ water and measured using a Dionex DX-600 ion chromatograph equipped with a 4 mm AS-9HC column. Reagents from the National Research Center for Certified Reference Materials (Beijing, China) were used as standards. Measurement of duplicate samples indicates the analytical error is less than 2%.

The samples for ammonium (NH₄⁺-N) concentration were diluted at 1:5 and determined using flow injection spectrophotometry in wavelength 543 nm, as described by Hall and Aller (1992). NH₄⁺-N standard solution was prepared using the NH₄⁺-N reference material (BWZ6768-2016). All standard solutions were appropriately diluted to generate a series of standard concentrations. Duplicate analysis after every 10 samples was performed to validate the porewater analysis procedure, and the reproducibility is better than ± 5%.

The CH₄ concentration was measured using the method of Jørgensen et al. (2001). The vial containing the sediment sample was shaken thoroughly to allow the porewater methane between the aqueous and gaseous phases to equilibrate. A 0.2-ml headspace gas sample was injected into a gas chromatograph (Agilent 6820). For porewater dissolved CH₄ concentration, the calculated CH₄ concentration per sediment volume is corrected by assuming a constant sediment porosity of 0.75. The two duplicate samples were measured with a precision of ± 3.0%.

The DIC concentration and its δ¹³C-DIC were analyzed with the 0.3 ml porewater samples according to the methods described by Liu et al. (2020a). The sealed porewater samples were acidified in precleaned extainers with 0.2 ml of 2 mol/l H₃PO₄, and the resulting CO₂ was purged from the samples. The DIC concentration and the

carbon isotopic composition of the CO_2 were measured using a Thermo Finnigan MAT 253 isotope ratio mass spectrometer coupled with a Thermo Finnigan Gasbench II. The DIC concentration was measured with a precision of $\pm 2\%$. The carbon isotopic ratios are reported in the standard δ notation concerning the Vienna PeeDee Belemnite (VPDB) standard and with both precision and accuracy of better than $\pm 0.15\%$ (1σ).

2.3.2 Solid sediment analysis

Sediment total organic carbon (TOC) and its stable isotopic values ($\delta^{13}\text{C}$ -TOC) were analyzed in duplicate, using an elemental analyzer (Vario EL III, Germany) connected to a continuous flow system (Isoprime 100), after removal of carbonate with HCl. The average standard deviations of the measurements were $\pm 0.2\%$ for TOC and $\pm 0.2\%$ for $\delta^{13}\text{C}$ -TOC. Weight percentages of total carbon (TC) were determined in duplicate (without acidification) by combustion (at 1000°C) on the elemental analyzer, and total inorganic carbon (TIC) was determined by difference: $\text{TIC} = \text{TC} - \text{TOC}$.

The X-ray diffraction (XRD) was performed to characterize the mineralogy of the powders of interest. Selected samples (55 cm, 415 cm, and 475 cm at site G16; 55 cm, 415 cm, and 535 cm at site G34; 55 cm, 355 cm and 775 cm at site G58) of 1.5 g were micronized under ethanol with a McCrone micronizing mill and then oven-dried at 60°C . After drying, the micronized samples were thoroughly mixed in an agate mortar and pestle to ensure homogeneity, followed by analyses using an X'pert Pro X-ray powder diffractometer (PANalytical, Netherlands) with $\text{Cu K}\alpha$ radiation at 40 kV and 40 mA. The measurements were carried out in the range of diffraction angles 2θ from 4° to 80° with a scanning step of 0.033° and rotation of the sample at a speed of 15 rpm. Qualitative and quantitative analyses

of minerals were performed using the software Profex (version 5.0.2) (Doebelin and Kleeberg, 2015).

Scanning electron microscopy (SEM) (Tescan Mira 3) with energy-dispersive X-ray microanalysis (EDX) (Oxford Ultim Max 40) was used to determine the morphology and elemental composition of the sites G16 and G34 samples because of their high level of carbonate content based on the XRD analysis (Supplementary Table S1). The freeze-dried subsamples were fixed onto aluminum stubs with two-way adherent tabs and allowed to dry overnight. Subsequently, the samples were sputter-coated with gold for 30 s. The SEM was operated at 2 kV with a working distance of 10 mm to facilitate optimum image collection while minimizing charging and sample damage. For EDX analysis, an accelerating voltage of 20 kV was used to generate sufficient X-ray counts.

3 Results

3.1 The depth profiles of porewater geochemistry

Figure 2 shows the depth profiles of the Cl^- , SO_4^{2-} , CH_4 and NH_4^+ concentrations in the porewater of Zone 1 and Zone 2. Porewater Cl^- concentration at all sampling sites remains almost constant and close to that in seawater. The SO_4^{2-} concentration decreases almost linearly with depth in Zone 1, and complete depletion occurs at around the depth of 400 cmbsf (centimeters below sea floor) ~ 500 cmbsf (SMT depth). By contrast, complete depletion of SO_4^{2-} concentration appears at around 1800 cmbsf at site G57 and 1100 cmbsf at site G58 in Zone 2. A noticeable increase

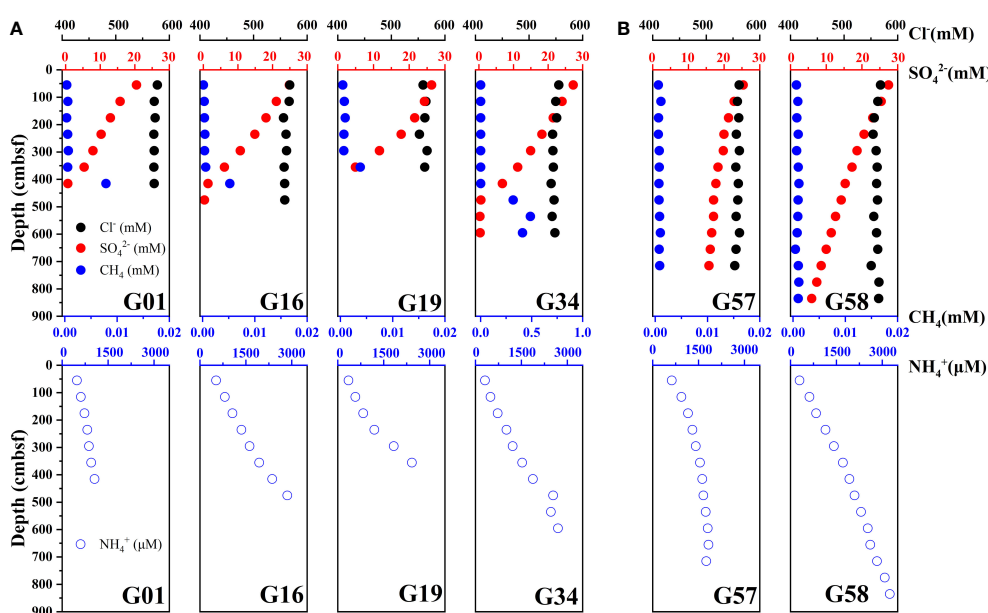


FIGURE 2

Down-depth profiles of porewater SO_4^{2-} , Cl^- , CH_4 and NH_4^+ in the sediments of the sites (A) G01, G16, G19, and G34 (Zone 1), and (B) G57, G58 (Zone 2).

in CH_4 concentration was observed around the SMT of the sites G01, G16, G19 and G34 in Zone 1, but CH_4 concentration is close to 0 and no change with depth at sites in Zone 2. The concentration of NH_4^+ ranges from 209.50 μM to 3243.00 μM , and an obvious negative correlation between the NH_4^+ and SO_4^{2-} in depth profiles occurs at all sites.

Depth profiles of the porewater Ca^{2+} , Mg^{2+} and Ba^{2+} are shown in Figure 3. The porewater Ca^{2+} concentrations at sites in Zone 1 and Zone 2 vary from 1.38 – 7.96 mM and 4.40 – 8.50 mM, respectively. The porewater Mg^{2+} concentrations are in the range of 37.76 – 55.91 mM and 50.64 – 56.33 mM at sites in Zone 1 and Zone 2. The concentrations of Ca^{2+} and Mg^{2+} decrease with depth in Zone 1, and their decreasing trends are more pronounced than those in Zone 2. The porewater Ba^{2+} concentrations at the sites of Zone 1 vary from 0.33 to 4.76 μM , and display a noticeable increasing trend below the depth of complete depletion of porewater sulfate. At the sites of Zone 2, however, the Ba^{2+} concentrations remain almost constant in the depth profiles, with a range of 0.35 to 0.54 μM .

The porewater DIC concentration increases with the depth, and the $\delta^{13}\text{C}$ -DIC values are negatively correlated with DIC concentration at all sites in Zone 1 (Figure 4A). The porewater DIC concentrations at sites G01, G16, G19 and G34 vary from 11.85 – 24.29 mM, 5.47 – 18.26 mM, 4.24 – 15.45 mM and 3.79 – 18.87 mM, and the $\delta^{13}\text{C}$ -DIC values range from –29.57 to –15.82 ‰, –35.04 to –15.70 ‰, –39.60 to –12.20 ‰ and –27.39 to –11.27 ‰, respectively. The most negative $\delta^{13}\text{C}$ -DIC occurs at the depth of maximum sulfate depletion. For site G58 in Zone 2 (Figure 4B), $\delta^{13}\text{C}$ -DIC values decrease almost linearly from –8.48‰ at the top to a minimum of –15.52‰ at the bottom. For site G57 in Zone 2 (Figure 4B), which has a much deeper SMT, the change in $\delta^{13}\text{C}$ -

DIC values is much more gradual since the site of AOM contributions to DIC is located deeper.

3.2 The depth profiles of sediment TOC, TIC and $\delta^{13}\text{C}$ -TOC

Figure 5 displays the depth profiles of sediment TOC, TIC and $\delta^{13}\text{C}$ -TOC. At the sites of Zone 1, the TOC shows a decreasing trend as depth increases, varying from 2.02% to 0.28%, while the TIC contents are in the range of 2.03% – 4.21% and exhibit a small increase trend with depth. In contrast, the TOC and TIC at site G58 in Zone 2 show small fluctuations in the depth profile, with ranges of 0.59% – 1.32% for TOC and 2.15% – 2.69% for TIC, respectively. At all sites, there is no clear trend of the $\delta^{13}\text{C}$ -TOC variation in the depth profile, and their values range from –24.14‰ to –20.59‰.

3.3 Morphology and mineralogy of the carbonate phase

Based on the vertical distribution of porewater geochemical profiles (Figures 2, 3), we selected the sediment samples from three different depths of Zone 1 (sites G16 and G34) and Zone 2 (site G58) for XRD analysis, and the results are shown in Figure 6 and Supplementary Table S1. Quantitative analyses of minerals were performed using the default structure repositories in the software Profex (version 5.0.2). Overall, the carbonates at sites G16, G34 and G58 are composed of calcite, aragonite, and dolomite. The percentage of each carbonate mineral within the bulk sediment and the relative abundance of each carbonate type in total

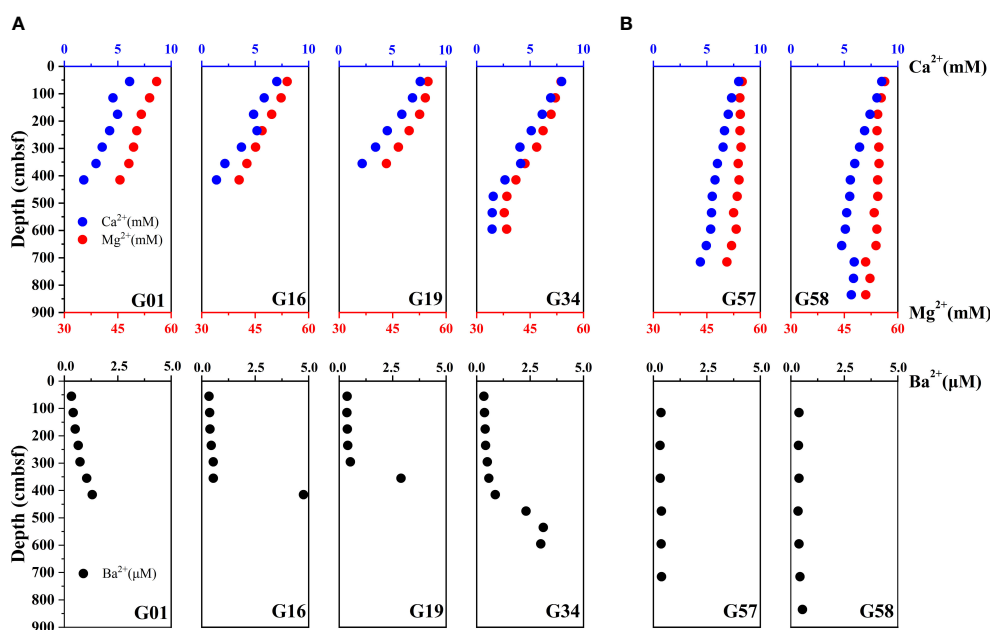


FIGURE 3

Down-depth profiles of porewater Ca^{2+} , Mg^{2+} and Ba^{2+} . (A) G01, G16, G19, and G34 (Zone 1), and (B) G57, G58 (Zone 2).

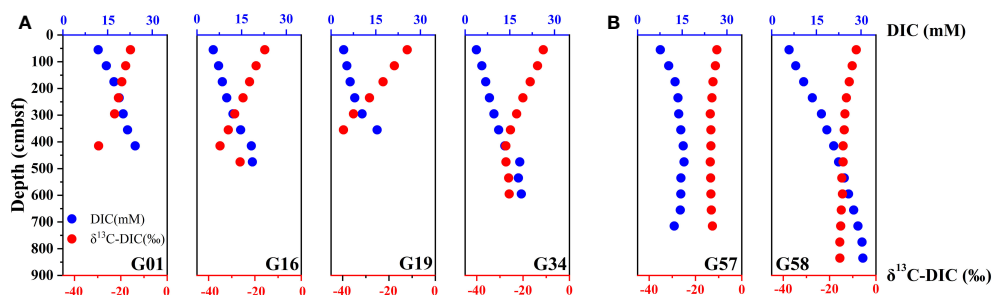


FIGURE 4

Down-depth profiles of porewater DIC and $\delta^{13}\text{C-DIC}$ in the sampling sites (A) G01, G16, G19, and G34 (Zone 1), (B) G57, G58 (Zone 2).

carbonates are listed in [Supplementary Table S2](#). By comparison, the ratio of calcite/ Σ carbonate is the highest in all selected samples (66.48% ~ 85.18% at site G16; 51.56% ~ 81.69% at site G34; 75.59% ~ 82.68% at site G58). Aragonite is almost undetectable in the shallow sediments (55 cmbsf depth) of sites G16 and G34 (aragonite/ Σ carbonate = 0), and not detected at all selected depths of site G58. The ratio of aragonite/ Σ carbonate decreases from 20.61% at 415 cmbsf depth to 6.94% at 475 cmbsf depth of site G16, and it increases dramatically from 4.50% at 415 cmbsf depth to 35.26% at 535 cmbsf depth of the site G34. However, the difference in the ratio of dolomite/ Σ carbonate is very small in all selected

samples (12.91% ~ 14.82% at site G16; 13.18% ~ 18.64% at site G34; 17.32% ~ 24.41% at site G58).

In addition to XRD analysis, the SEM images and EDS signals can also be utilized to identify the various carbonate phases. In this study, most of the carbonate concretions were observed in the deep layer of sites G16 and G34 ([Figure 7](#); [Supplementary Table S3](#)). The mineral morphology at the 415 cmbsf depth of site G16 is analogous to that at the 535 cmbsf depth of site G34. Both samples contain aragonite and calcite, where aragonite occurs in the habit of acicular CaCO_3 with roughly strip-shaped bodies ranging from 1 to 3 μm in diameter ([Figures 7B, G](#)), and calcite appears in a massive form ([Figures 7C,](#)

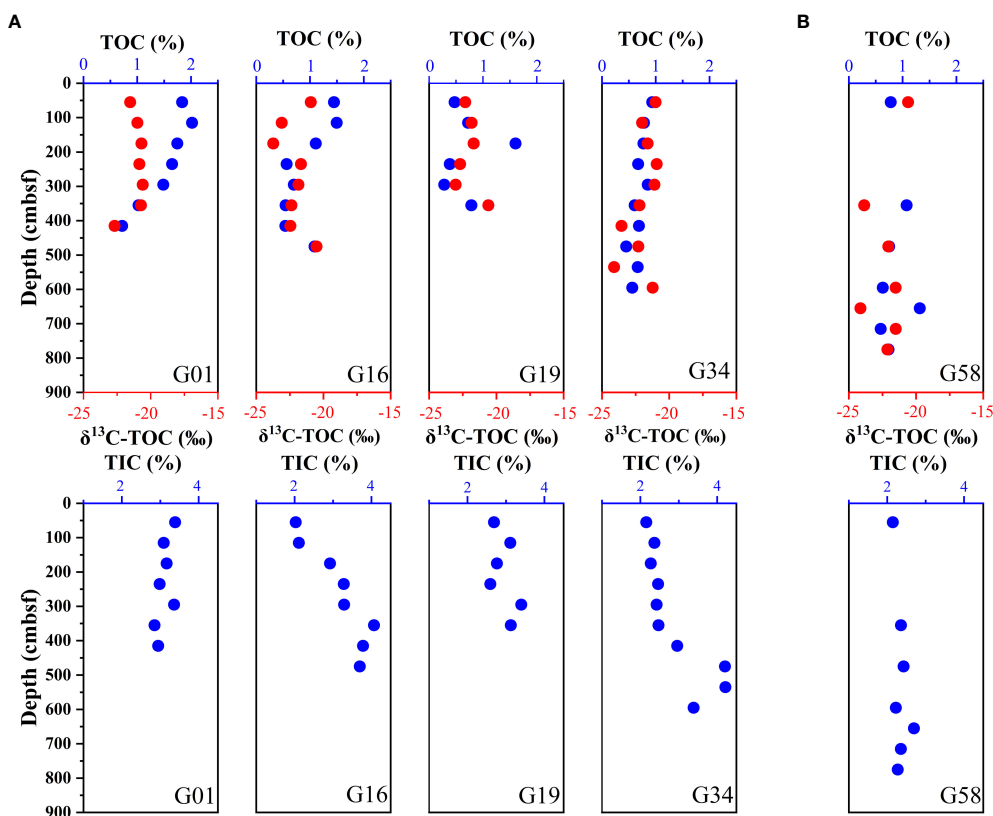
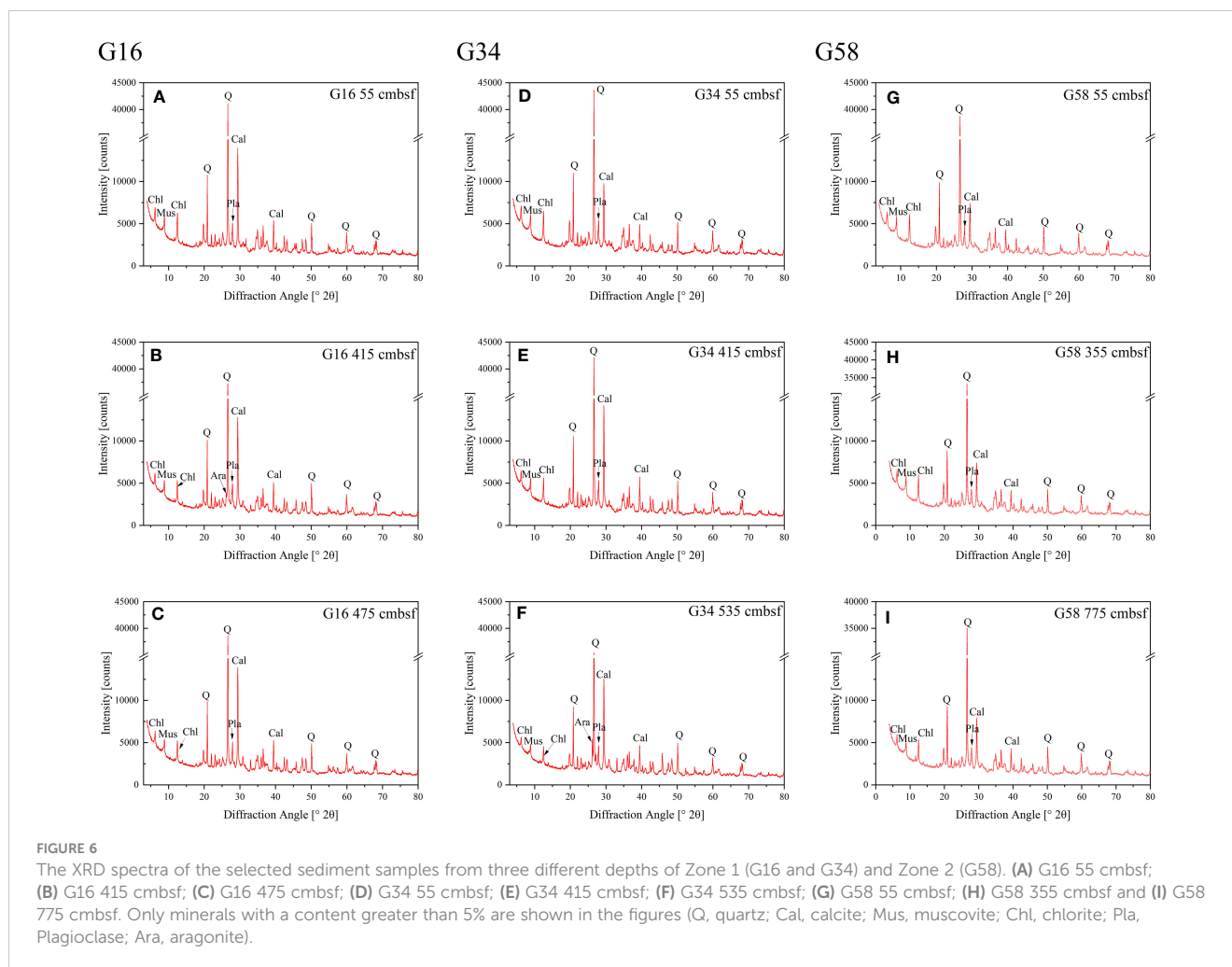


FIGURE 5

Down-depth profiles of sediment TOC, $\delta^{13}\text{C-TOC}$ and TIC. (A) G01, G16, G19, and G34 (Zone 1), (B) G58 (Zone 2).



H). At the other depths of the sites G16 and G34, no strip-shaped aragonite but only calcite was found (Figures 7A, D–F).

4 Modeling results of porewater geochemical profiles

The porewater geochemical profiles of sulfate, methane, calcium, magnesium, and DIC concentration were simulated by a reaction-transport model (RTM) under steady state (e.g., Berner, 1980; Chatterjee et al., 2011; Meister et al., 2019; Xu et al., 2023). The RTM was written using MATLAB R2023a and its code is provided in the Supplementary Material.

The instantaneous reaction rate equation (Equation 4) is as follows:

$$\frac{\partial(\phi \cdot C)}{\partial t} = \frac{\partial\left(\phi \cdot \frac{D_s(x)}{\tau^2} \cdot \frac{\partial C}{\partial x}\right)}{\partial x} - \frac{\partial(\phi \cdot \omega \cdot C)}{\partial x} + \phi \cdot \sum R(x, t) \quad (4)$$

where C is the concentrations, t is time, ω is the sedimentation rate, ϕ is the porosity of the marine sediment, D_s is the effective diffusion constant and is corrected by advection and tortuosity (τ^2) as $\tau^2 = 1 - 2 \ln \phi$ (Boudreau, 1997). The specific values of simulation

parameters are shown in Table 1, and part of the relevant data in the table refers to previous studies in this area (Luff et al., 2000; Hu et al., 2018).

The time of simulation is related to the sedimentation rate and porosity. Here we used an exponential function to describe porosity:

$$\phi(x) = \phi_0 \cdot e^{\lambda x} \quad (5)$$

where the value of porosity (ϕ_0) of sediment at the sediment-water interface (SWI) is set to 0.8, λ (-0.01) is the attenuation coefficient and x is the depth. The burial time can be calculated as (Meister et al., 2019):

$$t(x) = \int_0^x \omega^{-1} dx = \frac{\left[x - \frac{\phi_0}{\lambda} \cdot (e^{\lambda x} - 1)\right]}{\omega \cdot (1 - \phi_0)} \quad (6)$$

Sources and sinks of methane, sulfate, and DIC are stoichiometrically coupled to rates of organic matter (OM) degradation via the simplified reactions for sulfate reduction (SR) and methanogenesis (ME).

For OM degradation, the reactive continuum model (RCM) was applied (Boudreau and Ruddick B., 1991):

$$R_G(t) = -v \cdot (a + t)^{-1} \cdot G(t) \quad (7)$$

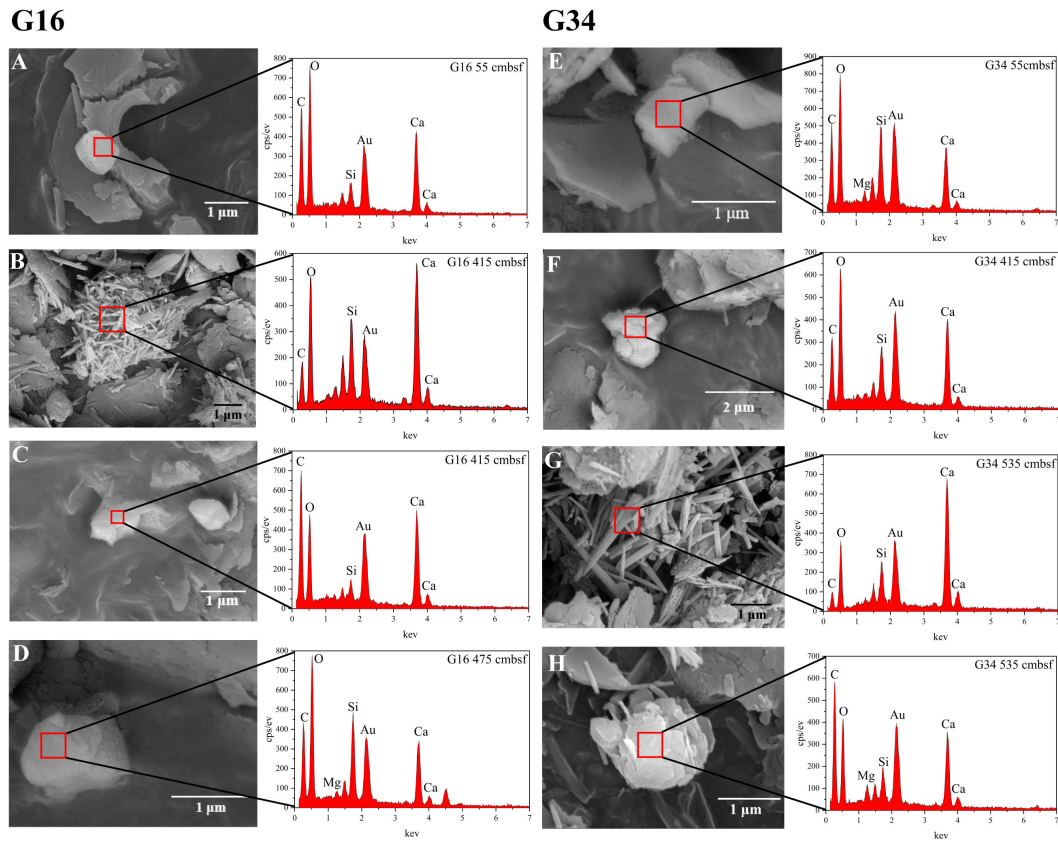


FIGURE 7 SEM images and EDS signals for sites G16 and G34. **(A)** Massive calcite at a depth of 55 cmbsf of site G16, **(B)** small loosely packed aragonite needle cluster with mainly long needles (1 ~ 3 μm) at a depth of 415 cmbsf of site G16, **(C)** the presence of calcite at a depth of 415 cmbsf of site G16, **(D)** calcite at a depth of 475 cmbsf of site G16, **(E)** massive calcite at a depth of 55 cmbsf of site G34, **(F)** a notable presence of calcite at a depth of 415 cmbsf of site G34, **(G)** the aragonite at a depth of 535 cmbsf of site G34, which is closely resembled that at a depth of 415 cmbsf of site G16, **(H)** calcite at a depth of 535 cmbsf of site G34.

where the parameter a describes the average lifetime of OM, ν defines the shape of the distribution, t is burial time calculated by Equation 6 and G represents the content of OM.

Based on the OM degradation rate, the SR and ME rates can be written as follows:

$$R_{SR} = \frac{1}{2} \cdot f_s \cdot R_{OM} \quad (8)$$

$$R_{ME} = \frac{1}{2} \cdot (1 - f_s) \cdot R_{OM} \quad (9)$$

where f_s is an error residual function (Chuang et al., 2019; Xu et al., 2023), as:

$$f_s = 0.5 \cdot \operatorname{erfc} \left(\frac{C_s - C_s^*}{b} \right) \quad (10)$$

where C_s is the sulfate concentration, C_s^* is the threshold sulfate concentration for methanogenesis (~ 1 mM), and b (~ 0.001) is a parameter controlling the steepness of f_s . When OM is degraded by OSR, $f_s = 1$; and when OM is degraded by methanogenesis, $f_s = 0$.

The ratio of DIC production from sulfate consumption via AOM is 1:1, and the rate of AOM can be described as:

$$R_{AOM} = k_{AOM} \cdot C_M \cdot C_S \quad (11)$$

where C_M is methane concentration, C_S is sulfate concentration and k_{AOM} is the first order rate constant for AOM.

The precipitation of carbonate is the sink of calcium and DIC (Equation 3), and its rate was calculated as Equation 12 (Luff et al., 2001):

$$R_{CA} = k_{Ca} \cdot \left(\frac{C_{calcium} \cdot C_{carbonate}}{K_{SP}^*} - 1 \right) \quad (12)$$

where $C_{calcium}$ and $C_{carbonate}$ represent the contents of calcium ions and carbonate, K_{SP}^* is the stoichiometric solubility constant of solid carbonate, k_{Ca} is the first-order kinetic rate constant for carbonate precipitation. The precipitation rate of magnesium (Mg^{2+}) in porewater is correlated with the precipitation rate of Ca^{2+} (Fantle and DePaolo, 2006; Fantle and DePaolo, 2007; Zhang and DePaolo, 2020), which can be written as following:

$$R_{Mg} = K_{Mg} \cdot \frac{C_{Mg}}{C_{Ca}} \cdot R_{cal} \quad (13)$$

TABLE 1 Model parameters and boundary conditions for the sediment cores in the study area.

Parameter	G01	G16	G19	G34	G57	G58	Source
Seafloor temperature (T, °C)	5.2	4.3	3.7	3.4	1.9	1.8	a
Salinity (S)	36.9	36.3	35.8	35.6	35.9	36.3	b
Pressure (P, MPa)	10.5	13.5	15.4	16.5	21.5	21.8	c
Density (ρ , kg/m ³)	2.6×10 ³	c					
Sedimentation rate (ω , cm/a)	4.2×10 ⁻³	3.8×10 ⁻³	3.4×10 ⁻³	3.5×10 ⁻³	2.9×10 ⁻³	2.8×10 ⁻³	d
Molecular diffusion coefficient of Sulfate (m ² /a)	1.8×10 ⁻²	e					
Molecular diffusion coefficient of Methane (m ² /a)	2.9×10 ⁻²	e					
Molecular diffusion coefficient of DIC (m ² /a)	1.9×10 ⁻²	e					
Molecular diffusion coefficient of Ca (m ² /a)	1.3×10 ⁻²	e					
Molecular diffusion coefficient of Mg (m ² /a)	1.2×10 ⁻²	e					
Upper boundary condition for sulfate (mM)	25	28	29	32	28	30	b
Upper boundary condition for methane	$\partial C/\partial X = 0$	b					
Upper boundary condition for DIC (mM)	9.1	2.1	2.1	2.1	5	3.5	b
Upper boundary condition for Ca (mM)	7	8	8.5	9.5	8	9.2	b
Upper boundary condition for Mg (mM)	58	56	56.5	56	56	56	b
Upper boundary condition for ¹³ DIC	-10	-5	-5	-7	-10	-5	b
Lower boundary condition for sulfate (mM)	$\partial C/\partial X = 0$	b					
Lower boundary condition for methane (mM)	8	8	10	10	/	/	b
Lower boundary condition for DIC	$\partial C/\partial X = 0$	b					
Lower boundary condition for Ca	$\partial C/\partial X = 0$	b					
Lower boundary condition for Mg	$\partial C/\partial X = 0$	b					
Upper boundary condition for ¹³ DIC	$\partial C/\partial X = 0$	b					

^aWu et al., 2021; ^bthis study; ^cBohrmann and cruise participants, 2008; ^dBoudreau, 1997; Luff et al., 2000.

The upper boundary of SO₄²⁻, Ca²⁺, $\delta^{13}\text{C}$ -DIC of the model was based on the porewater data of the shallowest sample, and DIC was derived from the modern seawater dataset (Meister et al., 2019). The lower boundary of SO₄²⁻, Ca²⁺, DIC, $\delta^{13}\text{C}$ -DIC, and the upper boundary of methane were designed as the Neumann boundary (the gradients of their concentrations were assumed to be zero) (Dale et al., 2019). The production and consumption of each dissolved species are based on reaction equations (Equations 1–3), and their rates were described as (Equations 7–16).

where C_{Mg} and C_{Ca} are the porewater concentrations of Mg²⁺ and Ca²⁺, and k_{Mg} is the first-order kinetic rate constant for magnesium precipitation.

The absolute concentrations of [¹³DIC] and [¹²DIC] were computed by separate reaction-transport (Equation 14) for each isotope ($R = R_{12} + R_{13}$). Minor carbon isotope fractionation occurs during OSR, AOM and carbonate precipitation (Meister et al., 2013; Chuang et al., 2019; Meister et al., 2019). Hence, the sources and sinks are assumed proportional to the isotopic composition of the source pool, and the rate of CH₄ can be calculated as follows:

$$\frac{R_{13\text{-AOM}}}{R_{12\text{-AOM}}} = \alpha_{\text{AOM}} \cdot R_{\text{CH}_4} \quad (14)$$

Methanogenesis can occur via two main pathways: the autotrophic pathway using CO₂ and H₂ and the acetoclastic pathway using acetate. However, independent of the pathway, the sources of methane and

DIC are in isotopic proportion with the OM by the fractionation factor α and $2-\alpha$, respectively (Meister et al., 2019).

$$\frac{R_{13}(\text{CH}_4)}{R_{12}(\text{CH}_4)} = \alpha_{\text{ME}} \cdot R_{\text{G}} \quad (15)$$

$$\frac{R_{13}(\text{DIC})}{R_{12}(\text{DIC})} = (2 - \alpha_{\text{ME}}) \cdot R_{\text{G}} \quad (16)$$

The concentration profiles of diverse species and R_{AOM} from Zone 1 and Zone 2 were simulated in this study. The modeling results are almost consistent with the measured concentrations of SO₄²⁻, Ca²⁺, and Mg²⁺ in Zone 1 and Zone 2 (Supplementary Table S4; Figure 8). By contrast, DIC concentration and $\delta^{13}\text{C}$ -DIC have a poor match with the simulated curve (Figure 8) and the possible explanation is that DIC samples undergo degassing during collection and storage, which will cause CaCO₃ to precipitate

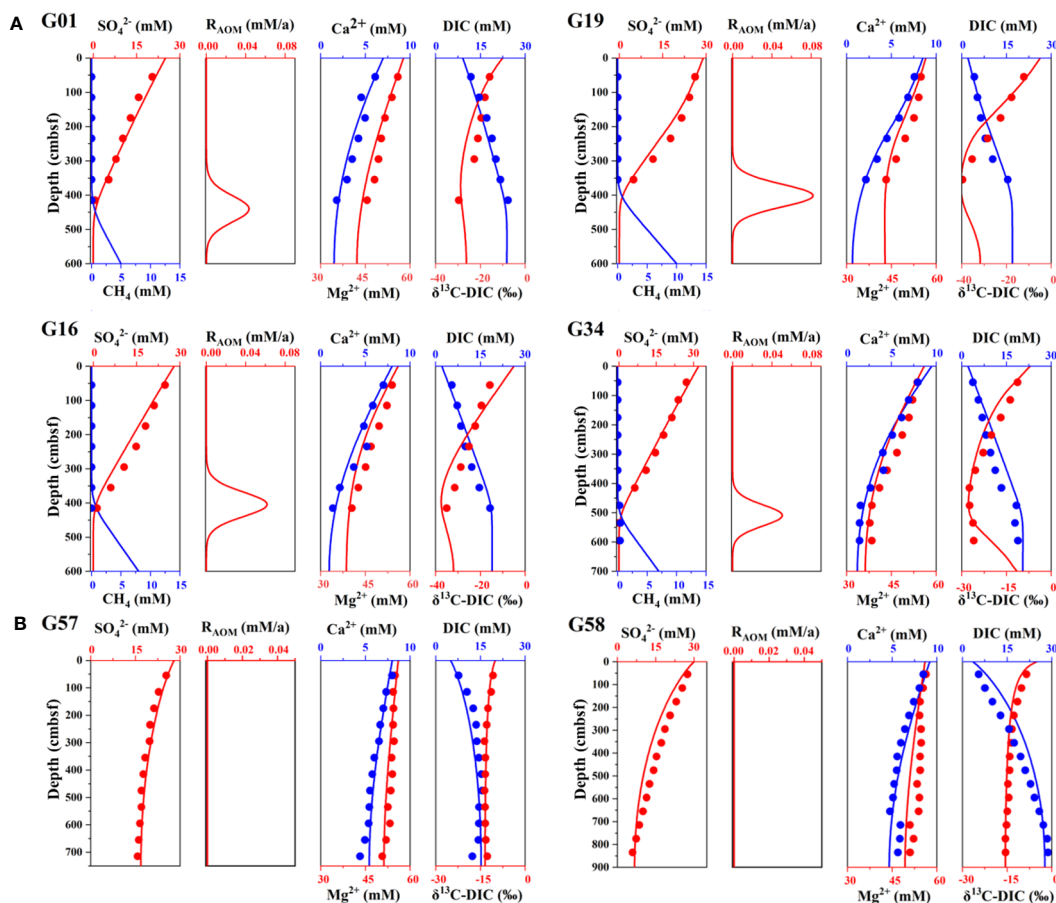


FIGURE 8

Measured (dots) and simulated (curves) depth profiles of the study sites (A) G01, G16, G19, and G34 (Zone 1) and (B) G57 and G58 (Zone 2). Down-depth profiles of SO_4^{2-} , CH_4 , R_{AOM} , Ca^{2+} , Mg^{2+} , DIC and $\delta^{13}\text{C-DIC}$ (‰). (The depth range of each site in the figure is different).

from the solution and lead to changes in physiochemical conditions (Miller et al., 2017).

Considering the uncertainty in methane sampling, the simulation of methane profiles is not only based on methane concentration profiles but also the porewater profiles of SO_4^{2-} and $\delta^{13}\text{C-DIC}$. As shown in Figure 8, the methane concentration at sites G01, G16, G19, and G34 in Zone 1 increases significantly at the bottom of sediments, while there is no methane occurring within the depth profiles of the sites G57 and G58 in Zone 2. In addition, the R_{AOM} of Zone 2 is zero and the decreasing trend of Ca^{2+} and Mg^{2+} is not as obvious as that of Zone 1. Based on the calculation of the reaction-transport model, site G19 has the highest value of R_{AOM} with $71.55 \text{ mmol/m}^2\text{-yr}$. Furthermore, the rates of authigenic carbonate precipitation are simulated as $7.54 \text{ mmol/m}^2\text{-yr}$ at site G01, $8.12 \text{ mmol/m}^2\text{-yr}$ at site G16, $7.20 \text{ mmol/m}^2\text{-yr}$ at site G19, and $10.11 \text{ mmol/m}^2\text{-yr}$ at site G34, respectively. In contrast, the rates of authigenic carbonate precipitation in Zone 2 are much lower than those in Zone 1. According to the OM degradation rate and calculation by the reaction-transport model (Equation 9), the methanogenesis rates at sites G01, G16, G19 and G34 are $1.70 \text{ mmol/m}^2\text{-yr}$, $2.30 \text{ mmol/m}^2\text{-yr}$, $1.40 \text{ mmol/m}^2\text{-yr}$ and $0.92 \text{ mmol/m}^2\text{-yr}$, respectively, however, the rates at sites G57 and G58 are nearly 0 (Supplementary Table S5).

5 Discussion

5.1 The relationship of the fluxes of DIC and SO_4^{2-} with SMT depth

The SMT, an important biogeochemical zone characterized by the simultaneous consumption of sulfate and methane (AOM, Equation 1), is commonly observed in methane-rich marine sediments at relatively shallow depths below the seafloor ($1 \sim 30 \text{ mbsf}$) (Malinverno and Pohlman, 2011). Within or near the SMT zone, the depletion of sulfate can lead to the dissolution of barite, thereby causing an increase in the concentration of porewater Ba^{2+} (Aloisi et al., 2004; Riedinger et al., 2006; Snyder et al., 2007). In this study, we also observed an increasing trend of Ba^{2+} concentration at or below the depth of SMT, but its concentration was relatively low, which may be mainly due to the lower content of barite minerals in the sediments (Supplementary Table S1). Here, we define the depth of SO_4^{2-} becomes near depleted (1 mM) as the SMT depth, which can be derived using the least square method by fitting the SO_4^{2-} depth profiles of all sampling sites (Borowski et al., 1999; Arndt et al., 2013; Chuang et al., 2016; Feng et al., 2018). When the sediment core sampling does not cross the SMT, the depth of the SMT can be achieved by extrapolating the SO_4^{2-} concentration

gradient to a depth where porewater SO_4^{2-} concentrations are near depleted (Smith and Coffin, 2014).

It should be noted that a shallow SMT often occurs a few centimeters below the seafloor with significant advection of upward fluids, such as seeps and vents, because the advecting fluids typically have a higher concentration of CH_4 than surrounding sediment, and advection often involves multiphase fluid flow (free gas and liquid) that may be episodic (Luff and Wallmann, 2003; Miller et al., 2017). However, the depths of SMT at our sampling sites are greater than 4 m and the porewater SO_4^{2-} concentrations exhibit a linear decrease in depth profiles, thereby suggesting that the impact of advection of upward fluids is not significant in this study area. Assuming under steady-state conditions, the diffusion rates of diverse species such as SO_4^{2-} , Ca^{2+} , Mg^{2+} and DIC, can be calculated from the linear fit to the species concentration (Supplementary Table S4) gradient according to Fick's first law (Equation 17) (e.g., Berner, 1978; Coffin et al., 2015):

$$J = -\phi \cdot D_s \cdot \frac{dc}{dx} \quad (17)$$

where J is the diffusive flux ($\text{mmol}/\text{m}^2 \text{ yr}$); ϕ is the porosity; D_s is the diffusion coefficient (m^2/s) which is related to temperature; c is the concentration of diverse species in pore water (mM), and x is the depth (mbsf). The bottom water temperatures at the study sites are shown in Table 1, and porosity is obtained by a functional relationship with depth (Equation 5). In this study, we set that the downward flux (SO_4^{2-}) is negative (into the sediments) corresponding to an upward flux (positive) for DIC out of the sediments. Due to the core sampling not crossing the SMT, it is difficult to estimate the flux of DIC upward from below the SMT. Nonetheless, our calculation results of the reaction-transport model show that the methanogenesis rate is much lower than the rates of AOM and OSR, indicating the flux of DIC from below SMT is much smaller than that from above SMT (Equation 9; Supplementary Table S5). Thus, the DIC_{net} flux is approximated as DIC diffusion upward through the sediments above the SMT (J_{DIC}) and the loss of DIC by authigenic carbonate precipitation (Table 2), where the loss

flux of DIC can be estimated using the porewater concentration profiles of Ca^{2+} and Mg^{2+} (Equation 18) (Smith and Coffin, 2014):

$$J_{\text{DIC}_{\text{net}}} = J_{\text{DIC}} + J_{\text{Mg}^{2+}} + J_{\text{Ca}^{2+}} \quad (18)$$

The fluxes of SO_4^{2-} and DIC_{net} in Zone 2 are significantly lower than those in Zone 1, and the larger fluxes of SO_4^{2-} and DIC_{net} correspond to the shallower SMT depth (Table 2). We combined the data from this study with the published data (Figure 9), and found that the DIC_{net} and SO_4^{2-} fluxes of all comparing sites have an exponential relationship with SMT depths ($y = 273.63x^{-1.17}$ and $y = -267.89x^{-1.37}$, Figure 9), which is very consistent with the report by Miller et al. (2017). The explanation for this correlation potentially lies in the fact that the fluxes of DIC and SO_4^{2-} to the SMT depth are mainly controlled by the reactivity and content of sediment OM in depth profiles (Egger et al., 2018; Xu et al., 2023). The diffusion flux of SO_4^{2-} is approximately equal to that of CH_4 within the SMT (Equation 1), so the depth of the SMT can provide a relatively qualitative prediction of upward CH_4 flux in the sediments.

5.2 Sulfate consumption pathways (OSR vs. AOM)

The depth profiles of porewater $\delta^{13}\text{C}$ -DIC exhibit the obvious characteristic pattern reflecting the occurrence of AOM. Especially, the minimum values of $\delta^{13}\text{C}$ -DIC (-27.40 ‰ to -39.60 ‰, Figure 4) at the depth of sulfate depletion are significantly more negative than that of the $\delta^{13}\text{C}$ of sedimentary OM found in this region (~ -21.0 ‰, von Rad et al., 1996). If only the degradation of organic carbon occurs within this depth range, then the $\delta^{13}\text{C}$ -DIC value should lie between that of seawater (0 ‰ PDB) and that of organic carbon (~ -21.0 ‰). Thus, the isotopic signature of DIC of this study indicates the additional source of light carbon in Zone 1 (Figure 4). The most likely source is AOM, which produces $\delta^{13}\text{C}$ -DIC that is isotopically lighter than that predicted from the simple mixing of the carbon derived from the OM degradation and seawater. Besides this, the

TABLE 2 SMT depth, sulfate diffusion rates ($J_{\text{SO}_4^{2-}}$), Ca^{2+} diffusion rates ($J_{\text{Ca}^{2+}}$), Mg^{2+} diffusion rates ($J_{\text{Mg}^{2+}}$) and DIC diffusion rates (J_{DIC}) at all sampling sites of methane-hydrate area in Makran continental margin.

Sample station	Water depth (m)	Core length (cm)	SMT depth (m)	$J_{\text{SO}_4^{2-}}$ ($\text{mmol}/\text{m}^2 \cdot \text{yr}$)	$J_{\text{Ca}^{2+}}$ ($\text{mmol}/\text{m}^2 \cdot \text{yr}$)	$J_{\text{Mg}^{2+}}$ ($\text{mmol}/\text{m}^2 \cdot \text{yr}$)	J_{DIC} ($\text{mmol}/\text{m}^2 \cdot \text{yr}$)	$J_{\text{DIC}_{\text{net}}}$ ($\text{mmol}/\text{m}^2 \cdot \text{yr}$)
Zone 1								
G01	844	415	4.12	-78.00	11.53	23.03	52.44	87.00
G16	1441	415	4.35	-92.68	14.34	32.23	45.64	92.21
G19	2214	355	4.32	-101.38	17.02	32.58	37.72	87.32
G34	2046	595	5.36	-77.82	12.76	28.92	37.61	79.30
Zone 2								
G57	3047	715	17.81	-16.63	3.88	4.20	22.83	30.92
G58	3102	835	10.23	-34.10	4.99	3.99	42.85	51.83

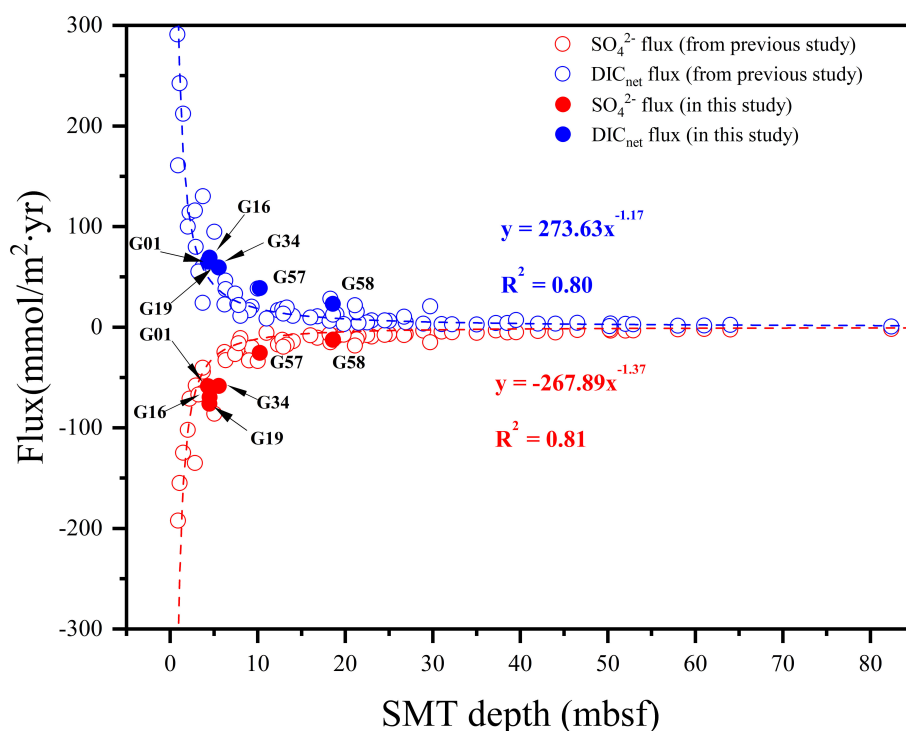


FIGURE 9

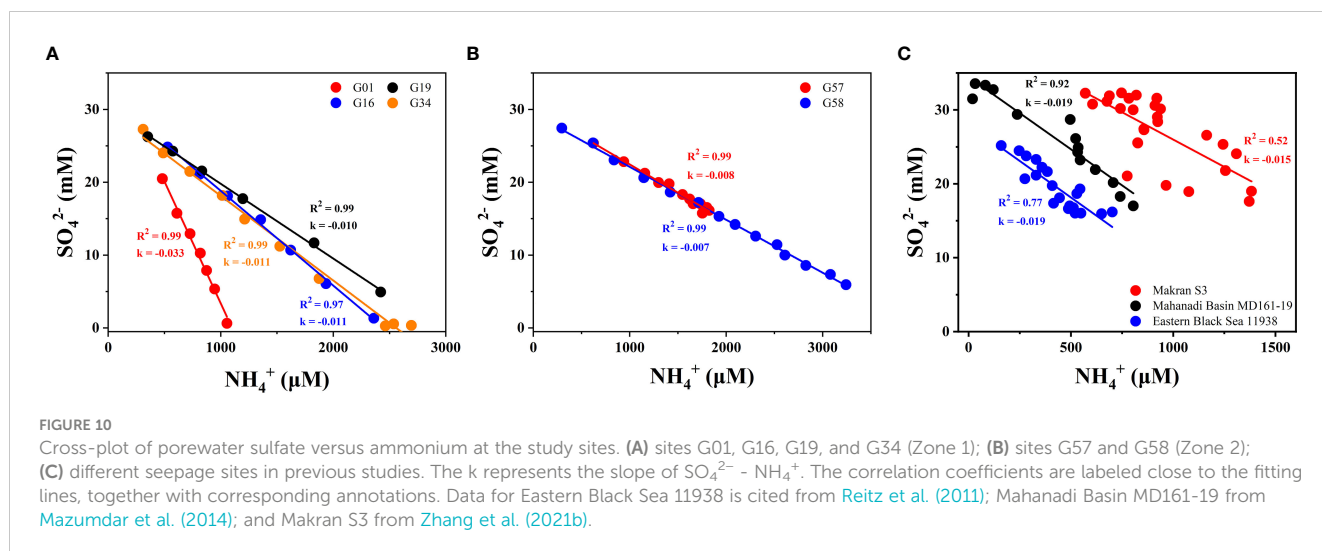
The exponential relationship of SO_4^{2-} and DIC_{net} flux with SMT depth. The data are sourced from the Makran accretionary wedge (Zhang et al., 2021b), Beaufort Sea (Coffin et al., 2013; Miller et al., 2017), East Siberian Slope (Miller et al., 2017), New Jersey Continental Slope (Berg, 2008), Blake Ridge (Paull et al., 1996; Keigwin et al., 1998; Berg, 2008), Gulf of Mexico (Kastner et al., 2008), Amazon Fan (Flood et al., 1995; Burns, 1998; Berg, 2008), Western Africa (Wefer et al., 1998; Berg, 2008), Oman (Berg, 2008), Bering Sea (Keigwin et al., 1998; Takahashi et al., 2011), Cascadia (Claypool et al., 2006; Dickens and Snyder, 2009), Umitaka Spur (Snyder et al., 2007), Japan Sea (D'Hondt et al., 2002), California Margin (Berg, 2008), Nankai Trough (Moore et al., 2001; Berg, 2008), Costa Rica Margin (Kimura et al., 1997; Berg, 2008), New Zealand (Hamdan et al., 2011; Coffin et al., 2014) and Antarctic (Geprägs et al., 2016), where the flux calculation results are cited from Miller et al. (2017).

decomposition of OM through bacterial sulfate reduction (OSR) can generate DIC and NH_4^+ and enter the surrounding porewater in the methane-bearing sediments (e.g., Luo et al., 2013; Zha et al., 2022), so NH_4^+ is an effective indicator of the extent of OM degradation because NH_4^+ is mainly produced via anaerobic bacterial decomposition of nitrogen-bearing organic compounds (Wehrmann et al., 2011; Mazumdar et al., 2014). It should be mentioned that the distribution of porewater NH_4^+ is influenced by many other factors. The first is the dilution of freshwater released by methane-hydrate decomposition. However, no significant fluctuations in Cl^- concentration were observed in the depth profiles, indicating that porewater NH_4^+ concentration is not affected by this effect. Secondly, methanogenesis in the sediments can also increase porewater NH_4^+ concentration (Mazumdar et al., 2014), but our results from the species concentration profiles and reaction-transport modeling confirm that the effect of deep methanogenesis is very limited (Supplementary Table S5). In addition, the temperature can affect ion diffusion and microbial-mediated OM decomposition, leading to changes in porewater NH_4^+ concentration in depth profiles (Sivan et al., 2007; Zhang et al., 2021b), but the temperature variation is very small due to a relatively short sediment core (< 8.5 m) in our sampling sites. Thus, the influence of temperature on NH_4^+ concentration can be ignored.

As shown in Figures 10A and B, the cross-plots of SO_4^{2-} vs. NH_4^+ display a significant negative relationship, indicating the OSR

process is accompanied by OM decomposition and NH_4^+ release in the study area. By comparison, the slope of SO_4^{2-} - NH_4^+ at site G01 ($k = -0.033$) is larger than those at all other sites (Figure 10), and the possible reason is due to the adsorption of NH_4^+ by clay minerals in the sediment at this site (Lukawska-Matuszewska and Kielczewska, 2016). Avinash et al. (2016) showed that the Arabian Sea sediments contain abundant illite with a large capacity for potassium-ammonium cation exchange, which originates from the fluvial or aeolian transport (wind-blown dust from the adjacent deserts). Therefore, we speculate that site G01 is more likely to receive abundant clay minerals like illite to absorb more NH_4^+ than other sites because it is located in a shallower water depth (844 m, Tabel 2). Although the OSR process occurs, our calculated flux of NH_4^+ (3.35 ~ 17.78 mmol/m²·yr) is much smaller than that of SO_4^{2-} (77.82 ~ 101.38 mmol/m²·yr), indicating that OSR does not play a dominant role in porewater sulfate reduction.

Distinguishing the relative contributions of OSR and AOM to sulfate consumption is crucial to accessing methane flux into the SMT and the associated biogeochemical processes occurring in marine sediments (Malinverno and Pohlman, 2011; Luo et al., 2013). In the reaction of AOM, the molecule ratio of the sulfate consumption vs. DIC generation is 1:1 on the basis of the chemical reaction formula (Equation 1), while in the OSR process, the consumption of one molecule of sulfate produces two molecules of DIC (Equation 2).



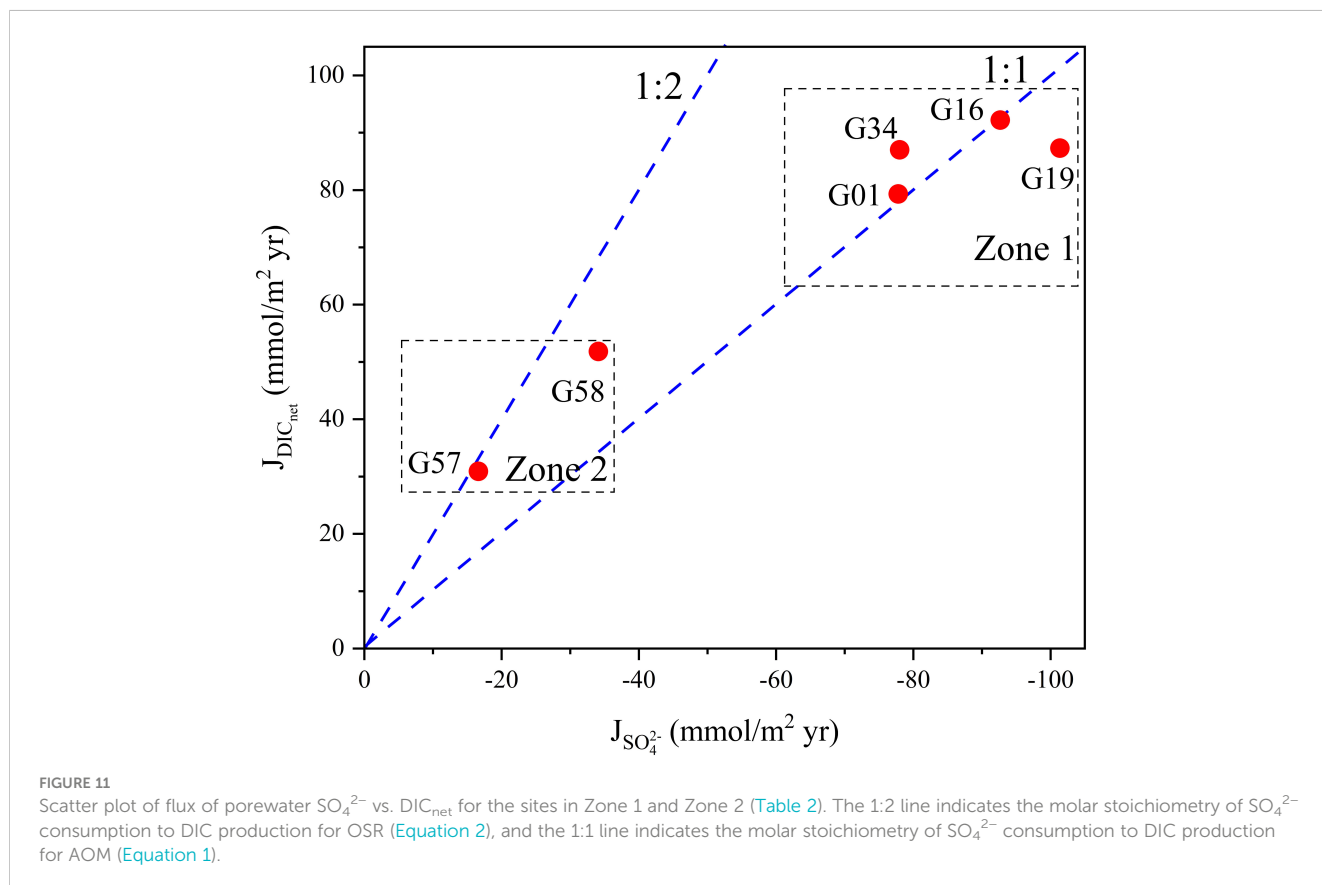
Therefore, the scatter plot of the flux of SO_4^{2-} vs. DIC_{net} can be used to estimate the relative contribution fractions of AOM and OSR to total porewater SO_4^{2-} consumption (Smith and Coffin, 2014).

As shown in Figure 11, dots of Zone 1 (G01, G16, G19 and G34) in the methane-hydrate area fall near the AOM line, indicating the AOM reaction is the major process for sulfate reduction (Akam et al., 2020; Zhang et al., 2021b). In comparison, dots of G57 and G58 of Zone 2 in the background area are closer to the OSR line, thus proving that OSR is the dominant process for sulfate consumption. This is further supported by simulation results from the reaction-

transport model, as the rates of AOM in Zone 1 are higher than those in Zone 2 (Figure 8; Supplementary Table S5).

5.3 Sources of porewater DIC

Porewater DIC mainly originates from AOM, OSR and the seawater that trapped during sediment accumulation (e.g., Borowski et al., 2000; Chatterjee et al., 2011; Feng et al., 2018; Meister et al., 2019; Akam et al., 2020). In some cases, the



incorporation of DIC from deep sediments may affect the $\delta^{13}\text{C}$ -DIC within the SMT (e.g., Chatterjee et al., 2011; Hu et al., 2022; Zha et al., 2022), but based on the modeling results of methane turnovers, the calculating depth-integrated AOM rates at sites G01, G16, G19 and G34 are about 25 to 51 times of the *in situ* methanogenesis rates (Supplementary Table S6). Therefore, *in situ* methanogenesis constitutes a minor proportion of the total DIC, whose effect on deep DIC production can thus be ignored in this study.

Here, an isotope mass balance model (Equation 19) was used to distinguish the source of porewater DIC in the closed systems (Borowski et al., 2000; Chen et al., 2010; Zhang et al., 2021b):

$$\delta^{13}\text{C}_{\text{DIC-added}} = (X_{\text{OM}}) * (\delta^{13}\text{C}_{\text{OM}}) + (X_{\text{AOM}}) * (\delta^{13}\text{C}_{\text{AOM}}) + (X_{\text{SW}}) * (\delta^{13}\text{C}_{\text{SW}}) \quad (19)$$

where X is the proportion of DIC from different sources, and $\delta^{13}\text{C}$ is the carbon isotope composition. The subscripts AOM, SW and OM refer to DIC derived from the sources listed above and the value of X_{SW} is obtained through dividing the DIC concentration of the overlying seawater by the DIC value within the SMT (Borowski et al., 2000). In this study, the average value of $\delta^{13}\text{C}$ -TOC for each core sediment is taken as the $\delta^{13}\text{C}_{\text{OM}}$. The $\delta^{13}\text{C}$ value of CH_4 (-68.5 ‰) is followed as reported by Römer et al. (2012). The $\delta^{13}\text{C}_{\text{DIC-added}}$ is defined as the isotopic value of the DIC being added to the initial porewater since the burial, which can be obtained from the slope of the linear regression graph of DIC vs. $\delta^{13}\text{C}$ -DIC*DIC (Ussler and Paull, 2008; Chen et al., 2010; Zhang et al., 2021b).

The $\delta^{13}\text{C}_{\text{DIC-added}}$ at sites G57 (-16.7 ‰) and G58 (-17.2 ‰) are more positive than $\delta^{13}\text{C}_{\text{OM}}$ (Figure 12B), indicating that the porewater DIC in Zone 2 is less affected by AOM. In Zone 1, however, the relative contributions of the AOM process to total porewater DIC are 60% at site G01, 52% at site G16, 68% at site G19,

and 25% at site G34 (Table 3). By comparison, the $\delta^{13}\text{C}$ -DIC_{added} value at site G34 (-31.6 ‰) is similar to that at site S3 in Makran from Zhang et al. (2021b) (-33.1 ‰) indicating that the two adjacent sites have the same DIC source (Figure 12A; Table 3). The difference in the percentage of porewater DIC sources at different sites is likely related to the flux of the upward diffusion of CH_4 in the methane-hydrate area (Chuang et al., 2013; Wei et al., 2019; Feng et al., 2020).

5.4 Removal of DIC by authigenic carbonate precipitation

The formation of authigenic carbonate is an important pathway to remove porewater DIC, particularly in continental shelf regions (e.g., Sun and Turchyn, 2014; Bradbury and Turchyn, 2019; Wang et al., 2019; Ruban et al., 2020; Loyd and Smirnov, 2022). In this study, porewater Ca^{2+} and Mg^{2+} concentrations decrease with depth, suggesting the authigenic carbonate precipitation at sites in the study area (Ritger et al., 1987; Aloisi et al., 2002; Snyder et al., 2007; Nöthen and Kasten, 2011). Numerical simulation by the reaction-transport model shows that the rate of authigenic carbonate precipitation is 10 $\text{mmol/m}^2\cdot\text{yr}$ at site G34, slightly higher than that at sites G01 (8 $\text{mmol/m}^2\cdot\text{yr}$), G16 (8 $\text{mmol/m}^2\cdot\text{yr}$), and G19 (7 $\text{mmol/m}^2\cdot\text{yr}$). The rates of authigenic carbonate precipitation at the sites in Zone 1 (average 8.25 $\text{mmol/m}^2\cdot\text{yr}$) are much higher than the global average (~ 5 $\text{mmol/m}^2\cdot\text{yr}$, Sun and Turchyn, 2014), emphasizing the significance of the methane hydrate area in the formation and burial of authigenic carbonate in global marine sediments. Compared with Zone 1, the rate of authigenic carbonates at sites G57 and G58 in the background area (Zone 2) is much lower (average 4 $\text{mmol/m}^2\cdot\text{yr}$).

The XRD analysis shows the mineral species of authigenic carbonate precipitation at sites G16, G34 and G58, which are

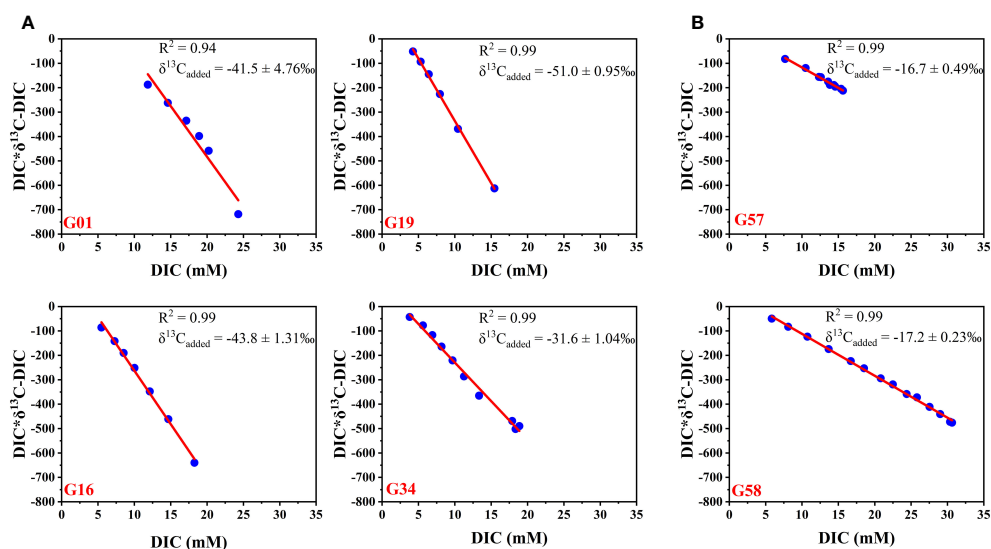


FIGURE 12

Linear regression diagrams of DIC vs. $\delta^{13}\text{C}$ -DIC*DIC at different sampling sites. (A) sites G01, G16, G19, and G34 (Zone 1); (B) sites G57 and G58 (Zone 2).

TABLE 3 The proportions of the various sources of DIC at different sampling sites.

Sample station	$\delta^{13}\text{C}_{\text{DIC-added}} (\text{‰})$	$\delta^{13}\text{C}_{\text{OM}} (\text{‰})$	$X_{\text{OM}} (\%)$	$\delta^{13}\text{C}_{\text{SW}} (\text{‰})$	$X_{\text{SW}} (\%)$	$\delta^{13}\text{C}_{\text{AOM}} (\text{‰})$	$X_{\text{AOM}} (\%)$
Zone 1							
G01	-41.5	-21.2	2	0	38	-68.5	60
G16	-43.8	-22.1	36	0	12	-68.5	52
G19	-51.0	-22.0	20	0	12	-68.5	68
G34	-31.6	-22.0	65	0	10	-68.5	25
Zone 2							
G57	-16.7	-22.2	ND	0	ND	-68.5	0
G58	-17.2	-22.2	ND	0	ND	-68.5	0
Makran							
S3	-33.1	-21.0	63	0	7	-68.5	30

ND means not determined. The data of site S3 is cited from Zhang et al. (2021b). The values of $\delta^{13}\text{C}_{\text{SW}}$ were estimated to be 0 ‰V-PDB refer to Zhang et al. (2021b).

mainly composed of calcite, aragonite, and dolomite (Figure 6; Supplementary Table S1). The molar fraction of MgCO_3 in calcite can be obtained by lattice parameters of calcite (Titschack et al., 2011; Dos Santos et al., 2017; Fahad and Saeed, 2018). Based on the XRD/Rietveld analysis, we found that the molar fraction of MgCO_3 in calcite is less than 10% at all sites in our study, indicating the absence of high-Mg calcite (Supplementary Table S6). In Zone 1, authigenic carbonate phases exhibit notable variations at different depths (Supplementary Table S1; Figure 6) of sites G16 and G34. At the surface sediments (55 cmbsf depth), calcite is the main component of carbonate phases, and aragonite is almost undetectable. However, the highest aragonite content occurs around the SMT with a depth of 415 cmbsf at site G16 (5.27%) and 535 cmbsf at site G34 (12.09%) (Supplementary Table S1), resulting in the highest ratio of aragonite/ Σ carbonate and the lowest ratio of calcite/ Σ carbonate appear at the SMT depth (Supplementary Table S2; Supplementary Figure S1). Many factors, such as sulfate inhibition and the presence of extracellular polymeric substances (EPS), can affect the formation of carbonate mineral phases (e.g., Formolo et al., 2004; Himmler et al., 2015; Li et al., 2018; Wang et al., 2019). Based on the results of porewater DIC and XRD analysis, however, we speculate that the solubility of carbonate minerals may play a significant role in the aragonite precipitation. According to carbonate solubility, calcite ($K' = 7.98 \times 10^{-7}$ at 5°C in 34.5‰ seawater) precipitation takes priority over aragonite ($K' = 11.4 \times 10^{-7}$ at 5°C in 34.5‰ seawater) (Berner, 1976). Therefore, at surface depth with relatively low DIC concentrations, calcite precipitates first. With the increase of DIC generated by the microbial-mediated AOM occurring around SMT depth (Chafetz et al., 1991; Peckmann et al., 2001; Liu et al., 2016), aragonite starts to precipitate, leading to the highest ratio of aragonite/ Σ carbonate around the SMT depth compared to other depths. Nevertheless, this ratio remains lower than that of calcite/ Σ carbonate at all depths. By contrast, aragonite does not appear while calcite is the dominant carbonate phase in Zone 2 (site G58) (Supplementary Tables S1, S2), which is similar to the distribution of carbonate phases in surface sediments of Zone 1, as it is less

affected by AOM (Liu et al., 2016; Li et al., 2018; Wei et al., 2020). Although dolomite is one of the carbonate phases in the study area, its content is relatively low (Zone 1: 2.73% ~ 4.47% at site G16; 2.47% ~ 4.52% at site G34; Zone 2: 2.52% ~ 3.10% at site G58) (Supplementary Table S1). Currently, the formation mechanism of dolomite is very complex and remains elusive (Cai et al., 2021). Microbially-mediated dolomite precipitation could possibly occur in modern reductive saline and anoxic environments (Warren, 2000; Cai et al., 2021), such as lagoons and gas hydrate areas (e.g., Casado et al., 2014; Li et al., 2018). Therefore, we infer that it is possible in the past that the accumulation of gas hydrates resulted in saline, sulfate-free porewaters which could host the small amounts of dolomite that we observed in this study.

5.5 Release of DIC to the overlying seawater

Theoretically, DIC that is not precipitated into authigenic carbonates can enter the upper sediment and eventually the overlying seawater through advection or diffusion (Chatterjee et al., 2011; Rassmann et al., 2018; Akam et al., 2020; Zhao et al., 2020). Based on extensive seafloor observations and geochemical analysis, methane hydrate systems contribute considerable proportions of the local carbon budget to the overlying seawater by emitting a large amount of DIC (Aharon et al., 1992; Suess et al., 1999; Garcia-Tigeros and Kessler, 2018; Feng et al., 2020). DIC released from marine sediments has an important influence on the carbonate equilibrium system in seawater (Chen, 2002; Krumins et al., 2013; Akam et al., 2020; Feng et al., 2020). Previous studies have shown that global DIC flux released from sediments to overlying seawater averages 6.5 Tmol/yr (3.2 ~ 9.2 Tmol/yr), of which 98% is released from continental margin sediments with the depth of SMT less than 13 m, equivalent to approximately 20% of the global river DIC (~ 33 Tmol/yr) flowing into the ocean (Meybeck, 1993; Amiotte Suchet et al., 2003; Treude et al., 2005; Aufdenkampe et al., 2011; Egger et al., 2018; Akam et al., 2020).

TABLE 4 The calculated DIC fluxes of the Makran continental margin by simulation using the reaction-transport model.

Sample station	DIC _{OSR} (mmol/m ² ·yr)	DIC _{AOM} (mmol/m ² ·yr)	DIC _{total} (mmol/m ² ·yr)	DIC _{carbonate} (mmol/m ² ·yr)	DIC _{burial} (mmol/m ² ·yr)	DIC _{out} (mmol/m ² ·yr)
Zone 1						
G01	27	43	70	8	1	61
G16	21	57	78	8	0.7	69.3
G19	27	71	98	7	0.6	90.4
G34	15	47	62	10	0.7	51.3
Zone 2						
G57	27	0	27	4	0.4	22.6
G58	27	0	27	4	0.8	22.2

In this study, we use the reaction-transport model to quantitatively assess the DIC fluxes released from the sediments into the overlying seawater of the Makran continental margin (Table 4). In this calculation, DIC_{OSR}, DIC_{AOM} and DIC_{carbonate} are simulated by the rate of OM decomposition, the rate of AOM within SMT, and the depth profile of Ca²⁺ concentration, respectively. As described previously, the situ methanogenesis via shallow OM decomposition is very low (Supplementary Table S5), so the contribution of DIC generated through this process is not considered. The flux of DIC_{burial} is constrained by the sedimentation rate and DIC concentration (Zha et al., 2022), thus it can be estimated by the reaction-transport model (Table 4). Furthermore, the DIC released from sediment to overlying seawater can be defined as Equation 20 (Wallmann et al., 2008; Dickens and Snyder, 2009; Chatterjee et al., 2011; Solomon et al., 2014; Akam et al., 2020):

$$\text{DIC}_{\text{out}} = \text{DIC}_{\text{OSR}} + \text{DIC}_{\text{AOM}} - \text{DIC}_{\text{carbonate}} - \text{DIC}_{\text{burial}} \quad (20)$$

Based on the Equation 20, we find that DIC_{out} differs greatly between the site G19 (90.4 mmol/m²·yr) and G34 (51.3 mmol/m²·yr), although both sites are located in the methane-hydrate area (Figure 1). In addition, we compared the DIC_{out} values in Zone 1 (68 ± 14 mmol/m²·yr) and Zone 2 (22.4 mmol/m²·yr), and this difference is likely caused by the different DIC cycling patterns between the two Zones (Table 4; Figure 13). As shown in Table 4

and Figure 13, the DIC fluxes produced by AOM in Zone 1 is 55 ± 11 mmol/m²·yr, which is significantly higher than that in Zone 2 (DIC_{AOM} = 0). Although the rate of authigenic carbonate formation is also relatively high in Zone 1, the process of carbonate precipitation is insufficient to prevent the release of large amounts of DIC from the sediment into the overlying seawater. By comparison, the fluxes of DIC released from sediments range from 51.3 to 90.4 mmol/m²·yr in Zone 1, which is higher than those of other methane-hydrate areas, such as the Gulf of Mexico (9 ~ 33 mmol/m²·yr, Smith and Coffin, 2014), Dongsha area of the southern South China Sea (13.1 ~ 26.1 mmol/m²·yr, Chen et al., 2017), Shenhu area of the southern South China Sea (10.1 ~ 31.7 mmol/m²·yr, Wu et al., 2013), and Beikang Basin (32.3 ~ 50.1 mmol/m²·yr, Feng et al., 2018).

This upward DIC flux across the seafloor accounts for an average of 88% of the total DIC in Zone 1. Importantly, the process of AOM contributed a large proportion of DIC_{out} at sites G01, G16, G19, and G34 in Zone 1 (Table 4) due to the upward flux of CH₄. High rates of AOM can lead to an increase in DIC_{out} flux and total alkalinity (TA) in the overlying seawater (Akam et al., 2020; Zha et al., 2022), which is beneficial to reduce ocean acidification and increases the CO₂ absorption capacity of seawater (Chen, 2002; Krumins et al., 2013; Akam et al., 2020; Feng et al., 2020). In future, more related work on carbon cycling in methane-bearing sediments should be conducted to quantitatively assess the DIC and TA released from global marine

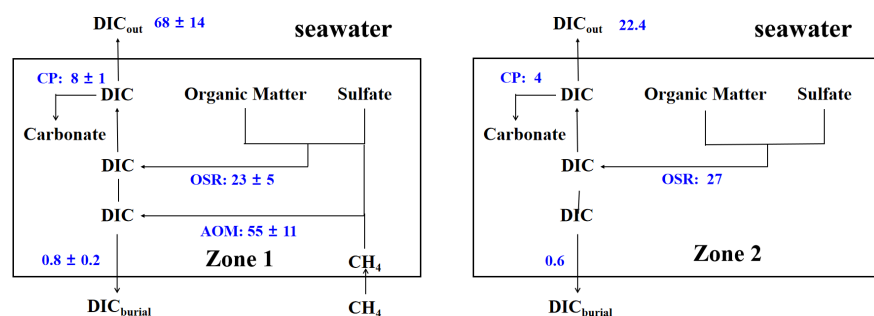


FIGURE 13

Two simplified schematics of the DIC release to the overlying seawater in Zone 1 and Zone 2. CP is the abbreviation for carbonate precipitation. The numbers represent the average flux and depth-integrated rates of DIC production and consumption in mmol/m²·yr of DIC.

sediments to the overlying seawater and their impact on carbonate equilibrium in marine systems.

6 Conclusion

Based on the active density of flares at the Makran continental margin, we divided the study area into Zone 1 (an active accretionary environment with high methane flux) and Zone 2 (a farther offshore background area). The differences in geological structures and sampling locations between the two zones have a potential impact on the porewater geochemistry and DIC flux. Our results show that Zone 1 has the larger CH_4 flux with the shallower SMT depth, and a noticeable increase in porewater Ba^{2+} concentration was observed within or near the SMT zone. The flux of SO_4^{2-} vs. DIC_{net} was used to determine the pathway of sulfate consumption at each site, revealing that almost all porewater SO_4^{2-} at sites G57 and G58 in Zone 2 is consumed by OSR, the AOM reaction, however, is the main process of sulfate consumption affected by methane diffusion at sites in Zone 1. The relative contributions of AOM to the porewater DIC calculated by the isotope mass balance model are 60% (G01) and 52% (G16), 68% (G19), and 25% (G34) in Zone 1, respectively. The TIC, XRD and SEM analyses show that the total carbonate content increases with depth, and the carbonate phases are composed of calcite, aragonite, and dolomite. By comparison, calcite is the main carbonate phase while the dolomite content is relatively low. Due to high concentration of DIC induced by AOM, aragonite appears at or below the depth of SMT. The reaction-transport model results and calculation reveal that the flux of DIC released from sediments is 51.3 to 90.4 $\text{mmol/m}^2\cdot\text{yr}$ in Zone 1, which is significantly higher than that in Zone 2 (22.4 $\text{mmol/m}^2\cdot\text{yr}$). Overall, this study highlights that the methane-related carbon pools are highly heterogeneous in the methane-hydrate area, and the contribution of AOM is essential to the authigenic carbonate burial and the bottom seawater chemistry.

Data availability statement

The raw data supporting the conclusions of this article will be made available by the authors, without undue reservation.

Author contributions

YC: Investigation, Formal analysis, Writing - Original Draft. SX: Formal analysis. WL: Investigation. JL: Resources, Investigation.

ZZ: Investigation. TY: Investigation. XX: Investigation. XD: Investigation. HY: Resources, Investigation, Conceptualization, Methodology. ZW: Conceptualization, Methodology, Writing - Review & Editing. All authors contributed to the article and approved the submitted version.

Funding

The author(s) declare financial support was received for the research, authorship, and/or publication of this article. This study was funded by the Development Program of China (No. 2022YFC2805400) and National Natural Science Foundation of China (No. 41976057, 42276059).

Acknowledgments

We thank reviewers and Editor Glen T. Snyder for their constructive comments and suggestions, which greatly helped us improve our manuscript. We also thank Dr. Zhe Zhou (Tongji University) for constructive comments on manuscript writing.

Conflict of interest

The authors declare that the research was conducted in the absence of any commercial or financial relationships that could be construed as a potential conflict of interest.

Publisher's note

All claims expressed in this article are solely those of the authors and do not necessarily represent those of their affiliated organizations, or those of the publisher, the editors and the reviewers. Any product that may be evaluated in this article, or claim that may be made by its manufacturer, is not guaranteed or endorsed by the publisher.

Supplementary material

The Supplementary Material for this article can be found online at: <https://www.frontiersin.org/articles/10.3389/fmars.2023.1181921/full#supplementary-material>

References

- Aharon, P., Graber, E. R., and Roberts, H. H. (1992). Dissolved carbon and $\delta^{13}\text{C}$ anomalies in the water column caused by hydrocarbon seeps on the northwestern Gulf of Mexico slope. *Geo-Marine Lett.* 12, 33–40. doi: 10.1007/BF02092106
- Akam, S. A., Coffin, R. B., Abdulla, H. A. N., and Lyons, T. W. (2020). Dissolved inorganic carbon pump in methane-charged shallow marine sediments: state of the art and new model perspectives. *Front. Mar. Sci.* 7. doi: 10.3389/fmars.2020.00206
- Aller, R. C., and Blair, N. E. (2004). Early diagenetic remineralization of sedimentary organic C in the Gulf of Papua deltaic complex (Papua New Guinea): Net loss of terrestrial C and diagenetic fractionation of C isotopes. *Geochim. Cosmochim. Acta* 68, 1815–1825. doi: 10.1016/j.gca.2003.10.028
- Aloui, G., Bouloubassi, I., Heijs, S., Pancost, R. D., Pierre, C., Sinninghe Damsté, J. S., et al. (2002). CH_4 -consuming microorganisms and the formation of carbonate crusts at cold seeps. *Earth Planet. Sci. Lett.* 203, 195–203. doi: 10.1016/S0012-821X(02)00878-6
- Aloui, G., Wallmann, K., Bollwerk, S. M., Derkachev, A., Bohrmann, G., and Stuess, E. (2004). The effect of dissolved barium on biogeochemical processes at cold seeps. *Geochim. Cosmochim. Acta* 68 (8), 1735–1748. doi: 10.1016/j.gca.2003.10.010
- Amiotte Suchet, P., Probst, J.-L., and Ludwig, W. (2003). Worldwide distribution of continental rock lithology: Implications for the atmospheric/soil CO_2 uptake by continental weathering and alkalinity river transport to the oceans. *Global Biogeochem. Cycles* 17 (2), 1038. doi: 10.1029/2002gb001891
- Arndt, S., Jørgensen, B. B., LaRowe, D. E., Middelburg, J., Pancost, R., and Regnier, P. (2013). Quantifying the degradation of organic matter in marine sediments: a review and synthesis. *Earth-sci. Rev.* 123, 53–86. doi: 10.1016/j.earscirev.2013.02.008
- Aufdenkampe, A. K., Mayorga, E., Raymond, P. A., Melack, J. M., Doney, S. C., Alin, S. R., et al. (2011). Riverine coupling of biogeochemical cycles between land, oceans, and atmosphere. *Front. Ecol. Environ.* 9, 53–60. doi: 10.1890/100014
- Avinash, K., Kurian, P. J., Warriar, A. K., Shankar, R., Vineesh, T. C., and Ravindra, R. (2016). Sedimentary sources and processes in the eastern Arabian Sea: Insights from environmental magnetism, geochemistry and clay mineralogy. *Geosci. Front.* 7, 253–264. doi: 10.1016/j.gsf.2015.05.001
- Berg, R. D. (2008). *Diffusional methane fluxes within continental margin sediments and depositional constraints on formation factor estimates*, (University of California, San Diego).
- Berner, R. A. (1976). The solubility of calcite and aragonite in seawater at atmospheric pressure and 34.5‰ salinity. *Am. J. Sci.* 276 (6), 713–730. doi: 10.2475/ajs.276.6.713
- Berner, R. A. (1978). Sulfate reduction and the rate of deposition of marine sediments. *Earth Planet. Sci. Lett.* 37 (3), 492–498. doi: 10.1016/0012-821x(78)90209-1
- Berner, R. A. (1980). *Early Diagenesis: A Theoretical Approach (No.1)*. (Princeton University Press). doi: 10.1515/9780691209401
- Boetius, A., Ravensschlag, K., Schubert, C. J., Rickert, D., Widdel, F., Gleske, A., et al. (2000). A marine microbial consortium apparently mediating AOM. *Nature* 407, 623–626. doi: 10.1038/35036572
- Borowski, W. S., Hoehler, T. M., Alperin, M. J., Rodriguez, N. M., and Paull, C. K. (2000). Significance of anaerobic methane oxidation in methane-rich sediments overlying the Blake Ridge gas hydrates. *Proc. Ocean Drill. Progr. Sci. Results* 164, 87–99. doi: 10.2973/odp.proc.sr.164.214.2000
- Borowski, W. S., Paull, C. K., and Ussler, W. (1996). Marine pore-water sulfate profiles indicate *in situ* methane flux from underlying gas hydrate. *Geology* 24, 655–658. doi: 10.1130/0091-7613(1996)024<0655:MPWSP>2.3.CO;2
- Borowski, W. S., Paull, C. K., and Ussler, W. (1999). Global and local variations of interstitial sulfate gradients in deep-water, continental margin sediments: Sensitivity to underlying methane and gas hydrates. *Mar. Geol.* 159, 131–154. doi: 10.1016/S0025-3227(99)00004-3
- Boudreau, B. P. (1997). *Diagenetic models and their implementation (Vol. 505)* (Berlin: Springer).
- Boudreau, B. P., and Ruddick, B. R. (1991). On a reactive continuum representation of organic matter diagenesis. *Am. J. Sci.* 291, 507–538. doi: 10.2475/ajs.291.5.507
- Bradbury, H. J., and Turchyn, A. V. (2019). Reevaluating the carbon sink due to sedimentary carbonate formation in modern marine sediments. *Earth Planet. Sci. Lett.* 519, 40–49. doi: 10.1016/j.epsl.2019.04.044
- Burns, S. J. (1998). Carbon isotopic evidence for coupled sulfate reduction-methane oxidation in Amazon Fan sediments. *Geochim. Cosmochim. Acta* 62, 797–804. doi: 10.1016/S0016-7037(98)00035-0
- Cai, W. K., Liu, J. H., Zhou, C. H., Keeling, J., and Glasmacher, U. A. (2021). Structure, genesis and resources efficiency of dolomite: New insights and remaining enigmas. *Chem. Geol.* 573, 120191. doi: 10.1016/j.chemgeo.2021.120191
- Casado, A. I., Alonso-Zarza, A. M., and La Iglesia, Á. (2014). Morphology and origin of dolomite in paleosols and lacustrine sequences. Examples from the Miocene of the Madrid Basin. *Sediment. Geol.* 312, 50–62. doi: 10.1016/j.sedgeo.2014.07.005
- Chafetz, H., Rush, P. F., and Utech, N. M. (1991). Microenvironmental controls on mineralogy and habit of CaCO_3 precipitates: an example from an active travertine system. *Sedimentology* 38, 107–126. doi: 10.1111/j.1365-3091.1991.tb01857.x
- Chatterjee, S., Dickens, G. R., Bhatnagar, G., Chapman, W. G., Dugan, B., Snyder, G. T., et al. (2011). Pore water sulfate, alkalinity, and carbon isotope profiles in shallow sediment above marine gas hydrate systems: A numerical modeling perspective. *J. Geophys. Res. Solid Earth* 116, 1–25. doi: 10.1029/2011JB008290
- Chen, C. T. A. (2002). Shelf-vs. dissolution-generated alkalinity above the chemical lysocline. *Deep. Res. Part II Top. Oceanogr.* 49 (24–25), 5365–5375. doi: 10.1016/S0967-0645(02)00196-0
- Chen, Y., Shen, L., Huang, T., Chu, Z., and Xie, Z. (2020). Transformation of sulfur species in lake sediments at Ardley Island and Fildes Peninsula, King George Island, Antarctic Peninsula. *Sci. Total Environ.* 703, 135591. doi: 10.1016/j.scitotenv.2019.135591
- Chen, T., Sun, X., Lin, Z., Lu, Y., Fang, Y., Wu, Z., et al. (2021). Deciphering the geochemical link between seep carbonates and enclosed pyrite: A case study from the northern South China sea. *Mar. Pet. Geol.* 128, 105020. doi: 10.1016/j.marpetgeo.2021.105020
- Chen, Y., Ussler, W., Haflidason, H., Lepland, A., Rise, L., Hovland, M., et al. (2010). Sources of methane inferred from pore-water $\delta^{13}\text{C}$ of dissolved inorganic carbon in Pockmark G11, offshore Mid-Norway. *Chem. Geol.* 275, 127–138. doi: 10.1016/j.chemgeo.2010.04.013
- Chen, N. C., Yang, T. F., Hong, W. L., Chen, H. W., Chen, H. C., Hu, C. Y., et al. (2017). Production, consumption, and migration of methane in accretionary prism of southwestern Taiwan. *Geochem. Geophys. Geosy.* 18, 2970–2989. doi: 10.1002/2017GC006798
- Chen, N., Yang, T. F., Liou, Y., Lin, H. T., Hong, W., Lin, S., et al. (2023). Controlling factors on patterns of dissolved organic carbon and volatile fatty acids in a submarine mud volcano offshore southwestern Taiwan. *Front. Earth Sci.* 11. doi: 10.3389/feart.2023.1210088
- Chuang, P. C., Dale, A. W., Wallmann, K., Haeckel, M., Yang, T. F., Chen, N. C., et al. (2013). Relating sulfate and methane dynamics to geology: Accretionary prism offshore SW Taiwan. *Geochem. Geophys. Geosy.* 14, 2523–2545. doi: 10.1002/ggge.20168
- Chuang, P. C., Yang, T. F., Wallmann, K., Matsumoto, R., Hu, C. Y., Chen, H. W., et al. (2019). Carbon isotope exchange during anaerobic oxidation of methane (AOM) in sediments of the northeastern South China Sea. *Geochim. Cosmochim. Acta* 246, 138–155. doi: 10.1016/j.gca.2018.11.003
- Chuang, P. C., Young, M. B., Dale, A. W., Miller, L. G., Herrera-Silveira, J. A., and Paytan, A. (2016). Methane and sulfate dynamics in sediments from mangrove-dominated tropical coastal lagoons, Yucatan, Mexico. *Biogeosciences* 13, 2981–3001. doi: 10.5194/bg-13-2981-2016
- Claypool, G. E., Milkov, A. V., Lee, Y. J., Torres, M. E., Borowski, W. S., and Tomaru, H. (2006). “Microbial Methane Generation and Gas Transport in Shallow Sediments of an Accretionary Complex, Southern Hydrate Ridge (ODP Leg 204), Offshore Oregon USA,” in *Proceedings of the ODP, Scientific Results*. Eds. A. M. Trehu, G. Bohrmann, M. E. Torres and F. S. Colwell (College Station, Texas: Ocean Drilling Program).
- Coffin, R. B., Hamdan, L. J., Smith, J. P., Rose, P. S., Plummer, R. E., Yoza, B., et al. (2014). Contribution of vertical methane flux to shallow sediment carbon pools across Porangahau Ridge, New Zealand. *Energies* 7, 5332–5356. doi: 10.3390/en7085332
- Coffin, R. B., Osburn, C. L., Plummer, R. E., Smith, J. P., Rose, P. S., and Grabowski, K. S. (2015). Deep sediment-sourced methane contribution to shallow sediment organic carbon: Atwater Valley, Texas-Louisiana Shelf, Gulf of Mexico. *Energies* 8, 1561–1583. doi: 10.3390/en8031561
- Coffin, R. B., Smith, J. P., Plummer, R. E., Yoza, B., Larsen, R. K., Millholland, L. C., et al. (2013). Spatial variation in shallow sediment methane sources and cycling on the Alaskan Beaufort Sea Shelf/Slope. *Mar. Pet. Geol.* 45, 186–197. doi: 10.1016/j.marpetgeo.2013.05.002
- D'Hondt, S., Rutherford, S., and Spivack, A. J. (2002). Metabolic activity of subsurface life in deep-sea sediments. *Science* 295 (5562), 2067–2070. doi: 10.1126/science.1064878
- Dale, A. W., Flury, S., Fossing, H., Regnier, P., Roy, H., Scholze, C., et al. (2019). Kinetics of organic carbon mineralization and methane formation in marine sediments (Aarhus Bay, Denmark). *Geochim. Cosmochim. Acta* 252, 159–178. doi: 10.1016/j.gca.2019.02.033
- Delisle, G., and Berner, U. (2002). Gas hydrates acting as cap rock to fluid discharge in the Makran accretionary prism? *Geol. Soc. Spec. Publ.* 195, 137–146. doi: 10.1144/GSL.SP.2002.195.01.09
- Dickens, G. R., and Snyder, G. T. (2009). Interpreting upward methane flux from marine pore water profiles. *Fire Ice* 9 (1), 7–10. Available at: <https://netl.doe.gov/sites/default/files/publication/MHNewsWinter09.pdf>.
- Doebelin, N., and Kleeberg, R. (2015). Profex: A graphical user interface for the Rietveld refinement program BGMN. *J. Appl. Crystallogr.* 48, 1573–1580. doi: 10.1107/S1600576715014685
- Dos Santos, H. N., Neumann, R., and Ávila, C. A. (2017). Mineral quantification with simultaneous refinement of Ca-Mg carbonates non-stoichiometry by X-Ray diffraction, rietveld method. *Minerals* 7, 164. doi: 10.3390/min7090164
- Egger, M., Riedinger, N., Mogollón, J. M., and Jørgensen, B. B. (2018). Global diffusive fluxes of methane in marine sediments. *Nat. Geosci.* 11, 421–425. doi: 10.1038/s41561-018-0122-8

- Fahad, M., and Saeed, S. (2018). Determination and estimation of magnesium content in the single phase magnesium-calcite $[Ca(1-x)Mg_xCO_3(s)]$ using electron probe micro-analysis (EPMA) and X-ray diffraction (XRD). *Geosci. J.* 22, 303–312. doi: 10.1007/s12303-017-0059-8
- Fantle, M. S., and DePaolo, D. J. (2006). S.R.X.X isotopes and pore fluid chemistry in carbonate sediment of the Ontong Java Plateau: Calcite recrystallization rates and evidence for a rapid rise in seawater Mg over the last 10 million years. *Geochim. Cosmochim. Acta* 70, 3883–3904. doi: 10.1016/j.gca.2006.06.009
- Fantle, M. S., and DePaolo, D. J. (2007). Ca isotopes in carbonate sediment and pore fluid from ODP Site 807A: The Ca^{2+} (aq)–calcite equilibrium fractionation factor and calcite recrystallization rates in Pleistocene sediments. *Geochim. Cosmochim. Acta* 71, 2524–2546. doi: 10.1016/j.gca.2007.03.006
- Feng, J., Li, N., Luo, M., Liang, J., Yang, S., Wang, H., et al. (2020). A quantitative assessment of methane-derived carbon cycling at the cold seeps in the northwestern south China sea. *Minerals* 10, 1–23. doi: 10.3390/min10030256
- Feng, D., Peng, Y., Bao, H., Peckmann, J., Roberts, H. H., and Chen, D. (2016). A carbonate-based proxy for sulfate-driven anaerobic oxidation of methane. *Geology* 44, 999–1002. doi: 10.1130/G38233.1
- Feng, J., Yang, S., Liang, J., Fang, Y., He, Y., Luo, M., et al. (2018). Methane seepage inferred from the porewater geochemistry of shallow sediments in the Beikang Basin of the southern South China Sea. *J. Asian Earth Sci.* 168, 77–86. doi: 10.1016/j.jseas.2018.02.005
- Fischer, D., Sahling, H., Nöthen, K., Bohrmann, G., Zabel, M., and Kasten, S. (2012). Interaction between hydrocarbon seepage, chemosynthetic communities, and bottom water redox at cold seeps of the Makran accretionary prism: Insights from habitat-specific pore water sampling and modeling. *Biogeosciences* 9, 2013–2031. doi: 10.5194/bg-9-2013-2012
- Flood, R. D., Piper, D. J. W., Klaus, A. Scientific Research Party. (1995). *Proceedings of the Ocean Drilling Program, Initial Reports*. (College Station, TX: Ocean Drilling Program), 155.
- Formolo, M. J., Lyons, T. W., Zhang, C., Kelley, C., Sassen, R., Horita, J., et al. (2004). Quantifying carbon sources in the formation of authigenic carbonates at gas hydrate sites in the Gulf of Mexico. *Chem. Geol.* 205, 253–264. doi: 10.1016/j.chemgeo.2003.12.021
- García-Tigueros, F., and Kessler, J. D. (2018). Limited acute influence of aerobic methane oxidation on ocean carbon dioxide and pH in hudson canyon, northern U.S. Atlantic margin. *J. Geophys. Res. Biogeosciences* 123, 2135–2144. doi: 10.1029/2018JG004384
- Geprägs, P., Torres, M. E., Mau, S., Kasten, S., Römer, M., and Bohrmann, G. (2016). Carbon cycling by methane seepage at the shallow Cumberland Bay, South Georgia, sub-Antarctic. *Geochem. Geophys. Geosy.* 17, 1401–1418. doi: 10.1002/2016GC006276
- Grando, G., and McClay, K. (2007). Morphotectonics domains and structural styles in the Makran accretionary prism, offshore Iran. *Sediment. Geol.* 196, 157–179. doi: 10.1016/j.sedgeo.2006.05.030
- Graves, C. A., Steinle, L., Rehder, G., Niemann, H., Connelly, D. P., Lowry, D., et al. (2015). Fluxes and fate of dissolved methane released at the seafloor at the landward limit of the gas hydrate stability zone offshore western Svalbard. *J. Geophys. Res.-Oceans* 120 (9), 6185–6201. doi: 10.1016/S0016-7037(03)00127-3
- Haas, A., Peckmann, J., Elvert, M., Sahling, H., and Bohrmann, G. (2010). Patterns of carbonate authigenesis at the Kouilou pockmarks on the Congo deep-sea fan. *Mar. Geol.* 268, 129–136. doi: 10.1016/j.margeo.2009.10.027
- Haese, R. R., Meile, C., Van Cappellen, P., and De Lange, G. J. (2003). Carbon geochemistry of cold seeps: Methane fluxes and transformation in sediments from Kagan mud volcano, eastern Mediterranean Sea. *Earth Planet. Sci. Lett.* 212, 361–375. doi: 10.1016/S0012-821X(03)00226-7
- Hall, P. O. J., and Aller, R. C. (1992). Rapid, small-volume, flow injection analysis for ΣCO_2 , and NH_4^+ in marine and freshwaters. *Limnol. Oceanogr.* 37, 1113–1119. doi: 10.4319/lo.1992.37.5.1113
- Hamdan, L. J., Gillevet, P. M., Pohlman, J. W., Sikaroodi, M., Greinert, J., and Coffin, R. B. (2011). Diversity and biogeochemical structuring of bacterial communities across the Porangahau ridge accretionary prism, New Zealand. *FEMS Microbiol. Ecol.* 77, 518–532. doi: 10.1111/j.1574-6941.2011.01133.x
- Himmler, T., Birgel, D., Bayon, G., Pape, T., Ge, L., Bohrmann, G., et al. (2015). Formation of seep carbonates along the Makran convergent margin, northern Arabian Sea and a molecular and isotopic approach to constrain the carbon isotopic composition of parent methane. *Chem. Geol.* 415, 102–117. doi: 10.1016/j.chemgeo.2015.09.016
- Hu, Y., Luo, M., Chen, L., Liang, Q., Feng, D., Tao, J., et al. (2018). Methane source linked to gas hydrate system at hydrate drilling areas of the South China Sea: Porewater geochemistry and numerical model constraints. *J. Asian Earth Sci.* 168, 87–95. doi: 10.1016/j.jseas.2018.04.028
- Hu, Y., Zhang, X., Feng, D., Peckmann, J., Feng, J., Wang, H., et al. (2022). Enhanced sulfate consumption fueled by deep-sourced methane in a hydrate-bearing area. *Sci. Bull.* 67, 122–124. doi: 10.1016/j.scib.2021.09.006
- Jørgensen, B. B., Beulig, F., Egger, M., Petro, C., Scholze, C., and Røy, H. (2019). Organoclastic sulfate reduction in the sulfate-methane transition of marine sediments. *Geochim. Cosmochim. Acta* 254, 231–245. doi: 10.1016/j.gca.2019.03.016
- Jørgensen, B. B., Weber, A., and Zopf, J. (2001). Sulphate reduction and anaerobic oxidation in Black Sea sediments. *Deep. Res. I* 48, 2097–2120. doi: 10.1016/S0967-0637(01)00007-3
- Kastner, M., Claypool, G., and Robertson, G. (2008). Geochemical constraints on the origin of the pore fluids and gas hydrate distribution at Atwater Valley and Keathley Canyon, northern Gulf of Mexico. *Mar. Pet. Geol.* 25, 860–872. doi: 10.1016/j.marpetgeo.2008.01.022
- Keigwin, L. D., Rio, D., Acton, G. D., and Shipboard Scientific Party. (1998). *Proceedings of the Ocean Drilling Program, Initial Reports*. (College Station, TX: Ocean Drilling Program), 172.
- Khan, M. J., Ali, M., Xu, M., and Khan, M. (2020). Seismicity analysis of selected faults in Makran Southern Pakistan. *Acta Geophys.* 68, 965–978. doi: 10.1007/s11600-020-00447-8
- Kimura, G., Silver, E. A., Blum, P., and Shipboard Scientific Party. (1997). *Proceedings of the Ocean Drilling Program, Initial Reports*, vol. 170.
- Knittel, K., and Boetius, A. (2009). Anaerobic oxidation of methane: Progress with an unknown process. *Annu. Rev. Microbiol.* 63, 311–334. doi: 10.1146/annurev.micro.61.080706.093130
- Kopp, C., Fruehn, J., Flueh, E. R., Reichert, C., Kukowski, N., Bialas, J., et al. (2000). Structure of the makran subduction zone from wide-angle and reflection seismic data. *Tectonophysics* 329, 171–191. doi: 10.1016/S0040-1951(00)00195-5
- Kretschmer, K., Biastoch, A., Rüpke, L., and Burwicz, E. (2015). Modeling the fate of methane hydrates under global warming. *Global Biogeochem. Cycles* 29, 610–625. doi: 10.1002/2014GB005011
- Krumins, V., Gehlen, M., Arndt, S., Van Cappellen, P., and Regnier, P. (2013). Dissolved inorganic carbon and alkalinity fluxes from coastal marine sediments: Model estimates for different shelf environments and sensitivity to global change. *Biogeosciences* 10, 371–398. doi: 10.5194/bg-10-371-2013
- Kvenvolden, K. A. (1988). Methane hydrate - A major reservoir of carbon in the shallow geosphere? *Chem. Geol.* 71, 41–51. doi: 10.1016/0009-2541(88)90104-0
- Lerche, I. (2000). Estimates of worldwide gas hydrate resources. *Energy Explor. Exploit.* 18, 329–337. doi: 10.1260/0144598001492157
- Li, N., Jin, M., Peckmann, J., Chen, D., and Feng, D. (2023). Quantification of the sources of sedimentary organic carbon at methane seeps: A case study from the South China Sea. *Chem. Geol.* 627, 121463. doi: 10.1016/j.chemgeo.2023.121463
- Li, J., Peng, X., Bai, S., Chen, Z., and Van Nostrand, J. D. (2018). Biogeochemical processes controlling authigenic carbonate formation within the sediment column from the Okinawa Trough. *Geochim. Cosmochim. Acta* 222, 363–382. doi: 10.1016/j.gca.2017.10.029
- Liao, J., Liu, X., Zhao, Q., Gong, J., Yin, W., Li, S., et al. (2022). Characteristics of high saturation hydrate reservoirs in the low-angle subduction area of the makran accretionary prism. *Front. Earth Sci.* 10. doi: 10.3389/feart.2022.861162
- Liu, S., Feng, X., Feng, Z., Xiao, X., and Feng, L. (2020b). Geochemical evidence of methane seepage in the sediments of the Qiongdongnan Basin, South China Sea. *Chem. Geol.* 543, 119588. doi: 10.1016/j.chemgeo.2020.119588
- Liu, W., Wu, Z., Xu, S., Wei, J., Peng, X., Li, J., et al. (2020a). Pore-water dissolved inorganic carbon sources and cycling in the shallow sediments of the Haima cold seeps, South China Sea. *J. Asian Earth Sci.* 201, 104495. doi: 10.1016/j.jseas.2020.104495
- Liu, X., Xu, T., Tian, H., Wei, M., Jin, G., and Liu, N. (2016). Numerical modeling study of mineralization induced by methane cold seep at the sea bottom. *Mar. Pet. Geol.* 75, 14–28. doi: 10.1016/j.marpetgeo.2016.04.010
- Lloyd, S. J., and Smirnov, M. N. (2022). Progressive formation of authigenic carbonate with depth in siliciclastic marine sediments including substantial formation in sediments experiencing methanogenesis. *Chem. Geol.* 594, 120775. doi: 10.1016/j.chemgeo.2022.120775
- Luff, R., Haeckel, M., and Wallmann, K. (2001). Robust and fast FORTRAN and MATLAB[®] libraries to calculate pH distributions in marine systems. *Comput. Geosci-UK* 27, 157–169. doi: 10.1016/S0098-3004(00)00097-2
- Luff, R., and Wallmann, K. (2003). Fluid flow, methane fluxes, carbonate precipitation and biogeochemical turnover in gas hydrate-bearing sediments at Hydrate Ridge, Cascadia Margin: Numerical modeling and mass balances. *Geochim. Cosmochim. Acta* 67, 3403–3421. doi: 10.1016/S0016-7037(03)00127-3
- Luff, R., Wallmann, K., Grandel, S., and Schlüter, M. (2000). Numerical modeling of benthic processes in the deep Arabian Sea. *Deep. Res. Part II Top. Stud. Oceanogr.* 47, 3039–3072. doi: 10.1016/S0967-0645(00)00058-8
- Lukawska-Matuszewska, K., and Kielczewska, J. (2016). Effects of near-bottom water oxygen concentration on biogeochemical cycling of C, N and S in sediments of the Gulf of Gdansk (southern Baltic). *Cont. Shelf Res.* 117, 30–42. doi: 10.1016/j.csr.2016.02.001
- Luo, M., Chen, L., Wang, S., Yan, W., Wang, H., and Chen, D. (2013). Pockmark activity inferred from pore water geochemistry in shallow sediments of the pockmark field in southwestern Xisha Uplift, northwestern South China Sea. *Mar. Pet. Geol.* 48, 247–259. doi: 10.1016/j.marpetgeo.2013.08.018
- Malinverno, A., and Pohlman, J. W. (2011). Modeling sulfate reduction in methane hydrate-bearing continental margin sediments: Does a sulfate-methane transition require anaerobic oxidation of methane? *Geochem. Geophys. Geosy.* 12, Q07006. doi: 10.1029/2011GC003501

- Mau, S., Römer, M., Torres, M. E., Bussmann, I., Pape, T., Damm, E., et al. (2017). Widespread methane seepage along the continental margin off Svalbard-from Bjørnøya to Kongsfjorden. *Sci. Rep.* 7, 1–13. doi: 10.1038/srep42997
- Mazumdar, A., Peketi, A., Joao, H. M., Dewangan, P., and Ramprasad, T. (2014). Pore-water chemistry of sediment cores off Mahanadi Basin, Bay of Bengal: Possible link to deep seated methane hydrate deposit. *Mar. Pet. Geol.* 49, 162–175. doi: 10.1016/j.marpetgeo.2013.10.011
- Meister, P., Liu, B., Ferdelman, T. G., Jørgensen, B. B., and Khalili, A. (2013). Control of sulphate and methane distributions in marine sediments by organic matter reactivity. *Geochim. Cosmochim. Acta* 104, 183–193. doi: 10.1016/j.gca.2012.11.011
- Meister, P., Liu, B., Khalili, A., Böttcher, M. E., and Jørgensen, B. B. (2019). Factors controlling the carbon isotope composition of dissolved inorganic carbon and methane in marine porewater: An evaluation by reaction-transport modelling. *J. Mar. Syst.* 200, 103227. doi: 10.1016/j.jmarsys.2019.103227
- Meybeck, M. (1993). Riverine transport of atmospheric carbon: sources, global typology and budget. *Water Air Soil Pollut.* 70, 443–463. doi: 10.1007/BF01105015
- Milkov, A. V. (2004). Global estimates of hydrate-bound gas in marine sediments: How much is really out there? *Earth-Science Rev.* 66, 183–197. doi: 10.1016/j.earscirev.2003.11.002
- Miller, C. M., Dickens, G. R., Jakobsson, M., Johansson, C., Koshurnikov, A., O'Regan, M., et al. (2017). Pore water geochemistry along continental slopes north of the East Siberian Sea: Inference of low methane concentrations. *Biogeosciences* 14, 2929–2953. doi: 10.5194/bg-14-2929-2017
- Moore, G. F., Taira, A., Klaus, A., and Shipboard Scientific Party. (2001). *Proceedings of the Ocean Drilling Program, Initial Reports*. Volume 190.
- Niewöhner, C., Hensen, C., Kasten, S., Zabel, M., and Schulz, H. D. (1998). Deep sulfate reduction completely mediated by anaerobic methane oxidation in sediments of the upwelling area off Namibia. *Geochim. Cosmochim. Acta* 62, 455–464. doi: 10.1016/S0016-7037(98)00055-6
- Nöthen, K., and Kasten, S. (2011). Reconstructing changes in seep activity by means of pore water and solid phase Sr/Ca and Mg/Ca ratios in pockmark sediments of the Northern Congo Fan. *Mar. Geol.* 287, 1–13. doi: 10.1016/j.margeo.2011.06.008
- Paull, C. K., Matsumoto, R., Wallace, P. J., and Shipboard Scientific Party. (1996). *Proceedings of the IODP, Initial Reports*. (College Station, TX, USA), Volume 164.
- Peckmann, J., Reimer, A., Luth, U., Luth, C., Hansen, B. T., Heinicke, C., et al. (2001). Methane-derived carbonates and authigenic pyrite from the northwestern Black Sea. *Mar. Geol.* 177, 129–150. doi: 10.1016/S0025-3227(01)00128-1
- Phrampus, B. J., and Hornbach, M. J. (2012). Recent changes to the Gulf Stream causing widespread gas hydrate destabilization. *Nature* 490, 527–530. doi: 10.1038/nature11528
- Rassmann, J., Lansard, B., Gazeau, F., Guidi-Guilvard, L., Pozzato, L., Alliouane, S., et al. (2018). Impact of ocean acidification on the biogeochemistry and meiofaunal assemblage of carbonate-rich sediments: Results from core incubations (Bay of Villefranche, NW Mediterranean Sea). *Mar. Chem.* 203, 102–119. doi: 10.1016/j.marchem.2018.05.006
- Reeburgh, W. S. (1976). Methane consumption in Cariaco Trench waters and sediments. *Earth Planet. Sci. Lett.* 28, 337–344. doi: 10.1016/0012-821X(76)90195-3
- Reitz, A., Pape, T., Haeckel, M., Schmidt, M., Berner, U., Scholz, F., et al. (2011). Sources of fluids and gases expelled at cold seeps offshore Georgia, eastern Black Sea. *Geochim. Cosmochim. Acta* 75, 3250–3268. doi: 10.1016/j.gca.2011.03.018
- Riedinger, N., Kasten, S., Gröger, J., Franke, C., and Pfeifer, K. (2006). Active and buried authigenic barite fronts in sediments from the Eastern Cape Basin. *Earth Planet. Sci. Lett.* 241, 876–887. doi: 10.1016/j.epsl.2005.10.032
- Ritger, S., Carson, B., and Suess, E. (1987). Methane-derived authigenic carbonates formed by subduction-induced pore-water expulsion along the Oregon/Washington margin. *Bull. Geol. Soc. Am.* 98, 147–156. doi: 10.1130/0016-7606(1987)98<147:MACFBS>2.0.CO;2
- Römer, M., Sahling, H., Pape, T., Bohrmann, G., and Spieß, V. (2012). Quantification of gas bubble emissions from submarine hydrocarbon seeps at the Makran continental margin (offshore Pakistan). *J. Geophys. Res.-Oceans* 117, C10015. doi: 10.1029/2011JC007424
- Ruban, A., Rudmin, M., Dudarev, O., and Mazurov, A. (2020). The formation of authigenic carbonates at a methane seep site in the northern part of the Laptev sea. *Minerals* 10, 1–14. doi: 10.3390/min10110948
- Schlüter, H. U., Prexl, A., Gaedicke, C., Roeser, H., Reichert, C., Meyer, H., et al. (2002). The Makran accretionary wedge: Sediment thicknesses and ages and the origin of mud volcanoes. *Mar. Geol.* 185, 219–232. doi: 10.1016/S0025-3227(02)00192-5
- Sivan, O., Schrag, D. P., and Murray, R. W. (2007). Rates of methanogenesis and methanotrophy in deep-sea sediments. *Geobiology* 5, 141–151. doi: 10.1111/j.1472-4669.2007.00098.x
- Smith, J. P., and Coffin, R. B. (2014). Methane flux and authigenic carbonate in shallow sediments overlying methane hydrate bearing strata in Alaminos Canyon, Gulf of Mexico. *Energies* 7, 6118–6141. doi: 10.3390/en7096118
- Snyder, G. T., Hiruta, A., Matsumoto, R., Dickens, G. R., Tomaru, H., Takeuchi, R., et al. (2007). Pore water profiles and authigenic mineralization in shallow marine sediments above the methane-charged system on Umitaka Spur, Japan Sea. *Deep. Res. Part II Top. Stud. Oceanogr.* 54, 1216–1239. doi: 10.1016/j.dsr2.2007.04.001
- Solomon, E. A., Spivack, A. J., Kastner, M., Torres, M. E., and Robertson, G. (2014). Gas hydrate distribution and carbon sequestration through coupled microbial methanogenesis and silicate weathering in the Krishna-Godavari Basin, offshore India. *Mar. Pet. Geol.* 58, 233–253. doi: 10.1016/j.marpetgeo.2014.08.020
- Suess, E. (2014). Marine cold seeps and their manifestations: geological control, biogeochemical criteria and environmental conditions. *Int. J. Earth Sci.* 103, 1889–1916. doi: 10.1007/s00531-014-1010-0
- Suess, E., Torres, M. E., Bohrmann, G., Collier, R. W., Greinert, J., Linke, P., et al. (1999). Gas hydrate destabilization: Enhanced dewatering, benthic material turnover and large methane plumes at the Cascadia convergent margin. *Earth Planet. Sci. Lett.* 170, 1–15. doi: 10.1016/S0012-821X(99)00092-8
- Sun, X., and Turchyn, A. V. (2014). Significant contribution of authigenic carbonate to marine carbon burial. *Nat. Geosci.* 7, 201–204. doi: 10.1038/ngeo2070
- Takahashi, K., Ravelo, A. C., Alvarez Zarikian, C. A. and the Expedition 323 Scientists. (2011). *Proceedings of the Integrated Ocean Drilling Program*, Volume 323.
- Titschack, J., Goetz-Neunhoffer, F., and Neubauer, J. (2011). Magnesium quantification in calcites [Ca, Mg]CO₃ by rietveld-based XRD analysis: Revisiting a well-established method. *Am. Mineral.* 96, 1028–1038. doi: 10.2138/am.2011.3665
- Treude, T., Niggemann, J., Kallmeyer, J., Wintersteller, P., Schubert, C. J., Boetius, A., et al. (2005). Anaerobic oxidation of methane and sulfate reduction along the Chilean continental margin. *Geochim. Cosmochim. Acta* 69, 2767–2779. doi: 10.1016/j.gca.2005.01.002
- Ussler, W., and Paull, C. K. (2008). Rates of anaerobic oxidation of methane and authigenic carbonate mineralization in methane-rich deep-sea sediments inferred from models and geochemical profiles. *Earth Planet. Sci. Lett.* 266, 271–287. doi: 10.1016/j.epsl.2007.10.056
- von Rad, U., Berner, U., Delisle, G., Doose-Rolinski, H., Fechner, N., Linke, P., et al. (2000). Gas and fluid venting at the Makran accretionary wedge off Pakistan. *Geo-Marine Lett.* 20, 10–19. doi: 10.1007/s003670000033
- von Rad, U., Rösch, H., Berner, U., Geyh, M., Marchig, V., and Schulz, H. (1996). Authigenic carbonates derived from oxidized methane vented from the Makran accretionary prism off Pakistan. *Mar. Geol.* 136, 55–77. doi: 10.1016/S0025-3227(96)00017-5
- Wallmann, K., Aloisi, G., Haeckel, M., Tishchenko, P., Pavlova, G., Greinert, J., et al. (2008). Silicate weathering in anoxic marine sediments. *Geochim. Cosmochim. Acta* 72, 2895–2918. doi: 10.1016/j.gca.2008.03.026
- Wang, M., Li, Q., Cai, F., Liang, J., Yan, G., Wang, Z., et al. (2019). Formation of authigenic carbonates at a methane seep site in the middle Okinawa Trough, East China Sea. *J. Asian Earth Sci.* 185, 104028. doi: 10.1016/j.jseas.2019.104028
- Warren, J. (2000). Dolomite: occurrence, evolution and economically important associations. *Earth Sci. Rev.* 52, 1–81. doi: 10.1016/S0012-8252(00)00022-2
- Wefer, G., Berger, W. H., Richter, C. Shipboard Scientific Party. (1998). *Proceedings of the Ocean Drilling Program, Initial Reports*. (College Station, TX: Ocean Drilling Program), 175, 487–504.
- Wehrmann, L. M., Risgaard-Petersen, N., Schrum, H. N., Walsh, E. A., Huh, Y., Ikehara, M., et al. (2011). Coupled organic and inorganic carbon cycling in the deep seafloor sediment of the northeastern Bering Sea Slope (IODP Exp.323). *Chem. Geol.* 284, 251–261. doi: 10.1016/j.chemgeo.2011.03.002
- Wei, J., Liang, J., Lu, J., Zhang, W., and He, Y. (2019). Characteristics and dynamics of gas hydrate systems in the northwestern South China Sea - Results of the fifth gas hydrate drilling expedition. *Mar. Pet. Geol.* 110, 287–298. doi: 10.1016/j.marpetgeo.2019.07.028
- Wei, J., Wu, T., Deng, X., Haider, S. W., Kahkashan, S., and Yang, S. (2021). Seafloor methane emission on the Makran continental margin. *Sci. Total Environ.* 801, 149772. doi: 10.1016/j.scitotenv.2021.149772
- Wei, J., Wu, T., Zhang, W., Deng, Y., Xie, R., Feng, J., et al. (2020). Deeply buried authigenic carbonates in the qiongdongnan basin, South China sea: Implications for ancient cold seep activities. *Minerals* 10, 1–19. doi: 10.3390/min10121135
- Winde, V., Böttcher, M. E., Escher, P., Böning, P., Beck, M., Liebezeit, G., et al. (2014). Tidal and spatial variations of $\delta^{13}\text{C}$ and aquatic chemistry in a temperate tidal basin during winter time. *J. Mar. Syst.* 129, 396–404. doi: 10.1016/j.jmarsys.2013.08.005
- Wu, T., Deng, X., Yao, H., Liu, B., Ma, J., Haider, S. W., et al. (2021). Distribution and development of submarine mud volcanoes on the Makran Continental Margin, offshore Pakistan. *J. Asian Earth Sci.* 207, 104653. doi: 10.1016/j.jseas.2020.104653
- Wu, L., Yang, S., Liang, J., Su, X., Fu, S., Sha, Z., et al. (2013). Variations of pore water sulfate gradients in sediments as indicator for underlying gas hydrate in Shenhu Area, the South China Sea. *Sci. China-Earth Sci.* 56, 530–540. doi: 10.1007/s11430-012-4545-6
- Wu, Z., Zhou, H., Ren, D., Gao, H., and Li, J. (2016). Quantifying the sources of dissolved inorganic carbon within the sulfate-methane transition zone in nearshore sediments of Qi'ao Island, Pearl River Estuary, Southern China. *Sci. China-Earth Sci.* 59, 1959–1970. doi: 10.1007/s11430-016-0057-0
- Xu, S., Liu, B., Wu, Z., Kowalski, N., and Böttcher, M. E. (2023). The role of anaerobic methane oxidation on the carbonate authigenesis in sediments of the subtropical Beibu Gulf, South China Sea: A reactive-transport modelling approach. *Chem. Geol.* 619, 121319. doi: 10.1016/j.chemgeo.2023.121319
- Zha, R., Yang, T., Shi, X., Su, P., and Fang, Y. (2022). Quantitative assessment of dissolved inorganic carbon cycling in marine sediments from gas hydrate-bearing areas

in the South China Sea. *Mar. Petrol. Geol.* 145, 105881. doi: 10.1016/j.marpetgeo.2022.105881

Zhang, S., and DePaolo, D. J. (2020). Equilibrium calcite-fluid Sr/Ca partition coefficient from marine sediment and pore fluids. *Geochim. Cosmochim. Acta* 289, 33–46. doi: 10.1016/j.gca.2020.08.017

Zhang, X., Gong, J., Sun, Z., Liao, J., Zhai, B., Wang, L., et al. (2021b). Pore-water geochemistry in methane-seep sediments of the Makran accretionary wedge off Pakistan: Possible link to subsurface methane hydrate. *Acta Oceanol. Sin.* 40, 23–32. doi: 10.1007/s13131-021-1899-7

Zhang, Z., He, G., Yao, H.-q., Deng, X., Yu, M., Huang, W., et al. (2020). Diapir structure and its constraint on gas hydrate accumulation in the Makran accretionary prism, offshore Pakistan. *China Geol.* 3, 611–622. doi: 10.31035/cg2020049

Zhang, W., Liang, J., Liang, Q., Wei, J., Wan, Z., Feng, J., et al. (2021a). Gas hydrate accumulation and occurrence associated with cold seep systems in the northern south China sea: an overview. *Geofluids* 2021, 1–24. doi: 10.1155/2021/5571150

Zhao, Y., Liu, J., Uthairan, K., Song, X., Xu, Y., He, B., et al. (2020). Dynamics of inorganic carbon and pH in a large subtropical continental shelf system: Interaction between eutrophication, hypoxia, and ocean acidification. *Limnol. Oceanogr.* 65, 1359–1379. doi: 10.1002/lno.11393